Item title: Optimal dynamic soaring consists of successive shallow arcs

Link back to the item: https://hdl.handle.net/1721.1/121512

Optimal dynamic soaring consists of successive shallow arcs

Gabriel D. Bousquet,[1*] Michael S. Triantafyllou,[1] Jean-Jacques E. Slotine[1]

[1]Department of Mechanical Engineering, Massachusetts Institute of Technology, Cambridge, MA 02139, USA.

*Corresponding author. E-mail: `g_b@mit.edu`

Albatrosses can travel a thousand kilometres daily over the oceans. They extract their propulsive energy from horizontal wind shears with a flight strategy called dynamic soaring. While thermal soaring, exploited by birds of prey and sports gliders, consists of simply remaining in updrafts, extracting energy from horizontal winds necessitates redistributing momentum across the wind shear layer, by means of an intricate and dynamic flight manoeuvre. Dynamic soaring has been described as a sequence of half-turns connecting upwind climbs and downwind dives through the surface shear layer. Here, we investigate the optimal (minimum-wind) flight trajectory, with a combined numerical and analytic methodology. We show that contrary to current thinking, but consistent with GPS recordings of albatrosses, when the shear layer is thin the optimal trajectory is composed of small-angle, large-radius arcs. Essentially, the albatross is a flying sailboat, sequentially acting as sail and keel, and most efficient when remaining crosswind at all times. Our analysis constitutes a general framework for dynamic soaring and more broadly energy extraction in complex winds. It is geared to improve the characterization of pelagic birds' flight dynamics and habitat, and could enable the development of a robotic albatross that could travel with a virtually infinite range.

1 Introduction

Dynamic soaring is the flight technique where a glider, either a bird a machine, extracts its propulsive energy from non-uniform horizontal winds such as those found over the oceans. Wandering albatrosses (*Diomedea exulans*), the archetypal dynamic soarers, have been recorded to travel 5,000 km per week while relying on wind energy alone [1–3]. The engineering potentialities of dynamic soaring are tantalizing: a robotic albatross could survey the oceans (or ride the wind shear of the jet stream [4]), and collect oceanic and atmospheric data, traveling at over 40 knots with a virtually infinite range [5, 6].

A major obstacle to intelligent robotic soaring resides in the complexity of the wind power extraction process that, by nature, requires planning on-the-go an energy positive trajectory in a stochastic, hard to measure, and poorly understood wind field. Conversely, progress in the description of dynamic soaring energetics can help design efficient algorithmic solutions to the online trajectory planning problem. Improving the understanding of dynamic soaring is also important in avian ecology. In particular, it allows to better evaluate the impact of climate change on the behaviour and habitat of albatrosses, petrels, and other pelagic birds, that are dependent on specific wind conditions [7].

At the mesoscale, it is known that the vast majority of the wandering albatross' flight is performed in an overall cross- or downwind direction, by dynamic soaring [3]. Although on relatively rare occasions (attributed to foraging [8]), they may fly upwind, in those instances they typically need to provide propulsive power. As far as dynamic soaring is concerned, crosswind flight (*i.e.* when the average airspeed is orthogonal to the average wind direction), is the dominant mode, and the focus of this paper.

In the first attempt to describe dynamic soaring, Rayleigh [9] modelled the wind profile (figure 1) as a still boundary layer separated from the above windy free stream blowing at W_0 by an infinitely thin shear layer (see figure 1*c*, hereafter Rayleigh's wind model). Rayleigh noticed that when traversing the shear layer up- or downwind, the albatross' groundspeed is conserved but its airspeed may increase by up to W_0. Rayleigh connected up- and downwind transitions with 180° half-turns in order to construct an energy neutral trajectory (hereafter Rayleigh's cycle, figure 2*b* and *e.g.* [10]): at each transition, the airspeed gain compensates for the inherent losses due to drag. Because the drag is quadratic with airspeed, a limit cycle is reached. This description of the dynamic soaring trajectory, based on phases of flight directly up- or downwind connected by half-turns, has carried on until today [10–21] in two energetically equivalent forms: trajectories with constant turn direction are O-shaped, or loitering; trajectories with alternating turn directions are S-shaped, or traveling.

Recently published observations based on high-accuracy GPS measurements [1, 22, 23] (reproduced in figures 2*a* and 3) show that albatrosses in crosswind flight do not follow half-turns, but rather an elongated, albeit oscillating, trajectory. As we report below, analysis of this data shows that they typically turn by only 50–70°, about a third of the Rayleigh's 180° half-turn.

The aim of this paper is to build a model of dynamic soaring that addresses the 3x factor discrepancy in turn amplitude between the half-turn explanation and published field data of flying albatrosses. To this end, we computed the "minimum-wind trajectory", *i.e.* the most efficient trajectory of dynamic soaring in the sense that it requires the least amount of wind to allow sustained flight, and we investigated the variation of its shape with the thickness of the shear layer. We discovered that contrary to prevailing theory, the most efficient trajectory in the thin shear layer regime is a sequence of arcs of vanishingly small angle, with the direction of flight nearly crosswind at all times. We were able to explain this observation analytically, lowering the wind required for dynamic soaring by over 35% compared to previous models [5].

2 Methods

2.1 Wind model

In the last two decades, a popular approach has consisted in pursuing accurate numerical modelling of the albatross flight in logarithmic or power-law wind profiles, deemed good models of the average wind field in the first 20 m above water, where the albatross flies. However, in this framework it has been shown [24, 25] that dynamic soaring is extremely sensitive to the wind field in the first meter above the surface, precisely where wind-wave interactions and temporal variability make the logarithmic model less relevant.

In contrast, Rayleigh's discontinuous wind model embraces the sharp wind shear that exists in separated regions, such as behind breaking waves or mountain ridges. Recent studies suggest that wind separation in ocean wave fields may be more frequent than previously believed ([26] and figure 1*a*), further reducing the relative merit of log-based descriptions.

In this study, rather than attempting to conduct high-fidelity, high-complexity modelling of dynamic soaring for a specific system, we aim for a general and robust analysis of the principles of dynamic soaring, the main conclusions of which should hold independently of the details of the wind field or glider. This approach is in part motivated by the fact that despite the significant stochasticity of the wind field in which albatrosses fly, their trajectory is quite regular. With this in mind, the wind profile, which varies with altitude z, is modelled by means of a logistic function (figure 1*b*) parameterized by the free stream wind speed W_0 and the shear layer thickness parameter δ

$$W(z) = \frac{W_0}{1 + \exp(-z/\delta)}. \tag{1}$$

This formulation, also suggested in [20] for modelling the wind field behind ridges, is intended to capture not only the main features of separated winds over ocean waves (see [10, 27, 28] for a qualitative discussion), but more generally of any flow with a typical wind inhomogeneity W_0 developing over a typical length-scale δ, such as in turbulence soaring [29, 30]. The regions of $z \ll -\delta$, $|z| \lesssim 3\delta$, $z \gg \delta$ represent a slow layer (separated region or boundary layer), shear layer of typical thickness $\Delta = 6\delta$, and windy free-stream layer, respectively. In the thin shear layer limit $\delta \to 0$ the model converges to Rayleigh's.

In a logarithmic profile (used to model attached flows), the boundary layer is both the slow layer and the shear layer. An assumption of our approach is that even logarithmic profiles have a characteristic shear layer thickness δ and a characteristic wind intensity W_0 such that equation (1) may be used to approximately represent those flows as well.

2.2 Equations of motion

We utilize a 3-degree-of-freedom model to represent the flight of an albatross or glider in a wind shear. Our formulation follows closely [5, 31] in the frame or reference $(\mathbf{i}, \mathbf{j}, \mathbf{k}) = (\mathbf{e}_{\text{East}}, \mathbf{e}_{\text{North}}, \mathbf{e}_{\text{Up}})$. Within this framework, six parameters fully define the glider's state: $\mathbf{x} = (V, \psi, \gamma, z, x, y)$. Here, V is the glider airspeed, and ψ and γ are the air-relative heading angle and air-relative flight path angle respectively. Specifically, ψ is the angle between $\mathbf{i}$ and the projection of the airspeed vector $\mathbf{V}$ in the $\mathbf{ij}$-plane and γ is the angle between $\mathbf{V}$ and the $\mathbf{ij}$-plane and is positive nose up. We assume that the wind is blowing from North to South when $W > 0$ *i.e.* $\mathbf{W}(z) = -W(z)\mathbf{j}$. The control inputs are the lift coefficient and bank angle $\mathbf{u} = (c_L, \phi)$.

The equations of motion (EOM) are:

$$m\dot{V} = -D - mg\sin\gamma + m\dot{W}\cos\gamma\sin\psi \tag{2a}$$

$$mV\dot{\gamma} = L\cos\phi - mg\cos\gamma - m\dot{W}\sin\gamma\sin\psi \tag{2b}$$

$$mV\dot{\psi}\cos\gamma = L\sin\phi + m\dot{W}\cos\psi \tag{2c}$$

$$\dot{z} = V\sin\gamma \tag{2d}$$

$$\dot{x} = V\cos\gamma\cos\psi \tag{2e}$$

$$\dot{y} = V\cos\gamma\sin\psi - W \tag{2f}$$

where the dots represent time derivation $\dot{V} = dV/dt$ and so on. Note that x, y in equations (2e) and (2f) may be considered as *outputs* rather than *states* as they do not feed back into the self-contained dynamics of equations (2a–2d). Following standard quasi-steady flight dynamics theory, lift and drag are specified according to $L = 1/2c_L\rho SV^2$ and $D = 1/2c_D\rho SV^2$. We assume quadratic drag $c_D = c_{D,0} + kc_L^2$. The coefficient $c_{D,0}$ represents the system's drag when no lift is generated and the parameter k expresses the additional generation of drag due to lift. Denoting $f \equiv c_L/c_D$ the glider's lift-to-drag ratio (or *finesse*), k is related to the maximum lift-to-drag ratio by $k^{-1} = 4f_{\max}^2 c_{D,0}$. For the numerical analysis below, $c_{D,0}$ and k are chosen such that the maximum lift-to-drag ratio $f_{\max}$ is reached at a lift coefficient of maximum glide ratio $c_{L,f_{\max}} = 0.5$, typical of a small glider.

2.3 Non-dimensionalisation

In order to compute the EOM numerically, and to obtain scale-invariant results, it is useful to rewrite equation (2) in non-dimensional form. For that purpose, the velocities are renormalized by the glider's characteristic speed at $c_L = 1$, namely $V_c = \sqrt{\frac{mg}{\frac{1}{2}\rho S}}$. The distances are renormalized by the characteristic length $\lambda = (V_c)^2/g$. Finally, time is renormalized by the time-scale $t_c = V_c/g = \lambda/V_c$. Note that our non-dimensionalisation depends only on the glider properties, air density, and gravity, arguably a more natural choice than approaches based on the wind gradient [31].

The speed V_c, directly related to the notion of "wing loading" (ratio between mass and wing area) expresses the order of magnitude of the airspeed at which the glider naturally flies. For instance, for a wandering albatross, $V_c = 15$ m/s (see section 2.5). Similarly, the length λ expresses what is a "small" or "large" change in altitude. For an albatross, $\lambda = 24$ m so a change of altitude of 2.4 m $\ll \lambda$ is "small" but a change of altitude of 240 m $\gg \lambda$ is "large". For a cruising A380 large passenger aircraft, $\lambda_{\mathrm{A380}} = 3.3$ km so an altitude change of 330 m is "small" but a change of altitude of 33 km is "large".

Upon non-dimensionalisation of the variables $v = V/V_c$, $w = W/V_c$, $\tilde{x} = x/\lambda$, $\tilde{y} = y/\lambda$, $\tilde{z} = z/\lambda$, $\tau = t/t_c$ and $(\cdot)' = d(\cdot)/d\tau$, equation (2) becomes

$$v' = -c_D v^2 - \sin\gamma + w' \cos\gamma \sin\psi \tag{3a}$$

$$v\gamma' = c_L v^2 \cos\phi - \cos\gamma - w' \sin\gamma \sin\psi \tag{3b}$$

$$v \cos\gamma \psi' = c_L v^2 \sin\phi + w' \cos\psi \tag{3c}$$

$$\tilde{z}' = v \sin\gamma \tag{3d}$$

$$w' = \frac{\partial w}{\partial \tilde{z}} \tilde{z}' \tag{3e}$$

$$\tilde{x}' = v \cos\gamma \cos\psi \tag{3f}$$

$$\tilde{y}' = v \cos\gamma \sin\psi - w. \tag{3g}$$

The non-dimensionalisation does not depend on the glider's characteristics except through the lift–drag coefficient curve $c_L \mapsto c_D$. For the remainder of this manuscript when there is no ambiguity the ˜ signs are omitted for notational simplicity.

2.4 Numerical trajectory optimization

A direct collocation method is applied to equation (3) with the wind model of equation (1), in order to compute the minimum-wind trajectory of dynamic soaring. Specifically, the aim is to find the minimum wind needed to sustain flight, *i.e.* the algorithm searches for the minimum wind intensity w_0 such that equation (3) has a solution periodic in $(v, \gamma, \psi + 2p\pi, z)$ with $p = 0, \pm 1$. More details on the procedure can be found in ST1 and *e.g.* [5, 24, 31]. The optimal loitering ($p = \pm 1$) and traveling trajectories ($p = 0$) are computed for several values of the shear layer thickness parameter δ, starting from a thick shear layer ($\delta \gg \lambda$) and reducing δ progressively until the thin shear layer regime ($\delta \ll \lambda$) is reached. The resulting trajectories are displayed in figure 4.

2.5 Dimensions for the wandering albatross' flight

Upon non-dimensionalisation in section 2.3, the trajectories that satisfy equation (3) are scale-independent. With the quantities below they may be rescaled to represent the conditions of the albatross' flight.

Albatross properties The typical properties for the wandering albatross are collected in table 1, and are used to convert the results of section 2.4 and the analytic analysis below back into dimensional form. Further information on mass and wing area of wandering albatrosses may be found in *e.g.* [7, 32]. To the best of our knowledge, the coefficient of minimum power $\left(c_L^{3/2}/c_D\right)_{\max}$, which is the important aerodynamic property for dynamic soaring ability in light winds as shown in equation (10) below, has not been specifically studied for the wandering albatross. For this study the numerical value 22 is chosen. It is similar to the 19.6 value from [5, 24], which is based of the simulation of a glider with size and planform similar to that of wandering albatrosses. It is also similar to the 22.9 value obtained by evaluating the quadratic drag formulation of [33] at a lift coefficient $c_L = 1.25$. Overall, we estimate the uncertainty over this coefficient to be approximately 10%, comparable to that on mass and wing area.

Wind properties The wind parameters δ and W_0 are more uncertain than the albatross' properties because the wind structure depends on the sea state, is complex and time-varying, and is poorly known overall.

The effective shear layer thickness perceived by the albatross must be at least of the order of the vertical distance from wingtip to wingtip when the albatross is in a roll. Given the wandering albatross' 3 m span, the perceived shear layer must be thicker than approximately 1 m. In the presence of large waves, Pennycuick's description of dynamic soaring as "gust soaring" at the interface between windy and separated regions behind waves [27] is indicative of a thin shear layer, of size comparable to the albatross'. Accordingly, observational data of flying albatrosses suggest a shear layer thickness of the order of 1–3 meters in the presence of waves. Conversely, when the waves are small and the wind flow remains attached to the surface, it is possible that the albatross does not have access to the extremely thin boundary layer and as a consequence perceives a virtually thicker shear layer. For logarithmic profiles, the perceived shear layer thickness would be approximately 7 m (see ST3). It is also possible to estimate the shear layer thickness indirectly form vertical travel reports of soaring albatrosses. The literature [1, 22, 27] suggests that over a dynamic soaring cycle, the albatross travels vertically by 5 to

15 m. The results of the numerical analysis of section 2.4 show that for the minimum-wind trajectory there is a correlation between vertical travel and shear layer thickness. Referring to figure 7*a*, such vertical travels correspond to a shear layer thickness of about 1.5 m to 7 m (3 m thickness for the 8 m vertical travel reported in [27]). Overall, considerations on separation behind waves, the albatross size, and albatross' vertical travel a suggest a shear layer thickness of the order of 1 to 3 meters (in this study we select 2 m as the default thickness), at the very maximum 7 m.

The intensity parameter W_0 in equation (1) does not necessarily denote the wind speed *stricto sensu*, but more precisely the speed difference between the fast and slow layers. For instance, the 7.8 m/s wind reported in figure 2*a* is the wind at 10m (see [22]). The speed of the slow layer is non-zero, as even behind separated waves, the mass of air typically travels at the wave phase speed [34]. Accordingly, the albatross can only exploit a fraction of the wind speed. Similarly, in non-separated flows the low-height wind at 1 m is typically more than 50% of the wind at 10 m and here again, only a relatively small fraction of the wind speed can be exploited [24]. In the present study we assume that the albatross may access 25 to 50% of the wind speed at 10 m.

2.6 Analysis of flight data from the literature

For wandering albatrosses in crosswind, the typical dynamic soaring manoeuvre lasts for 5–15 s and extends over 50–150 m, such that analysing the albatross' flight at the cycle level requires measuring its trajectory at a sampling rate of 1 Hertz or more. The present study reanalyses a short (3 km) track from Sachs *et al.* [22] with a high (10 Hz) sampling rate, and two long (order of 1,000 km) tracks from Yonehara *et al.* [23] sampled at a lower rate (1 Hz). Sachs' track [22] contains 20 soaring cycles while Yonehara's tracks [23] contains thousands of them. For each recording, characteristics of the flight are computed, *e.g.* cycle turn amplitude (see ST2 for more details on the procedure).

2.6.1 Albatross track in Sachs *et al.* [22]

The albatross track in Sachs *et al.* [22], reproduced in figure 2*a*, has two characteristics that make it well-suited for the present study: 1) the high sampling rate allows for reliable measurements of the small-scale features of individual turns and 2) the wind intensity, reported at 7.8 ± 2 m/s (see [22] and reference herein for methodology of determining the wind from satellite measurements), lies at the lower end of the wandering albatross' dynamic soaring flight envelope.

In this study, we discuss the dynamic soaring trajectory that minimizes the required wind. In practice, a flying albatross fulfils more complex objectives, for instance foraging, which may involve sub-objectives such as minimizing control effort, selecting cross-country average speed direction and altitude, *etc.* In particular, when the wind is plentiful, staying aloft is comparatively easy and it is less likely that the albatross' objective is to extract as much energy as possible. When the wind is weak however, it is likely that staying aloft becomes the albatross' main objective, as in our model. Accordingly, the low-wind of [22] is valuable as in it the albatross must pursue an objective similar to our computations. In the 20-cycle (40-turn) recording, the albatross' median turn is 54° (mean 50), with a standard deviation of 21° (see figures 2 and 6 and ST2).

2.6.2 Albatross tracks in Yonehara *et al.* [23]

Yonehara *et al.* [23, 35] contains two recordings of wandering albatrosses, reproduced in figure 3. Over the course of two days, albatross #2 performs "mixed" flights made of up-, cross- and downwind flights in low and high winds, separated by active foraging and resting periods. It has over 1,700 km of usable flight data and over 13,000 turns. Albatross #4 contains a nearly uninterrupted, generally westwards flight. In [35], the wind is measured with satellite data and estimated from the albatross track itself. Both methods suggest that overall the flight is approximately crosswind, in 8–15 m/s winds. It has 650 km of usable data in 3,700 turns, performed over the span of 9 hours. The median turn for albatross #2 in mixed flight is 78° (mean 84°, std 46°). The median turn for albatross #4 in crosswind flight is 66° (mean 69°, std 32°) (see figure 6 and ST2. For more details on the open-access dataset [23] and the in-flight wind conditions, see the supplementary materials of [35]).

3 Results

3.1 Three-dimensional minimum-wind trajectories in a logistic wind profile

Figure 4 shows the minimum-wind trajectory for three shear layer thicknesses (thick, albatross-like conditions, and thin). The main attributes of the cycle, spanning several orders of magnitude in shear layer thickness from $\delta \ll \lambda$ to $\delta \gg \lambda$ are displayed in figures 6 and 7.

When the shear layer is thick all trajectories are significantly three-dimensional, the loitering and traveling trajectories are quantitatively similar, and the turn amplitude of the traveling trajectory is large. When the shear layer is thin however the loitering and traveling trajectories are distinctly different. While the loitering trajectory remains significantly 3D, the traveling trajectory's extension in the z-direction shrinks and it becomes nearly 2D. As the shear layer thickness parameter δ is decreased, the trajectory becomes more and more elongated, and is composed of zigzags of only a few degrees in amplitude (figure 6*b*). Importantly, it requires only about 2/3 as much wind as the loitering trajectory (figure 6*a*).

3.2 Analytic solution in the thin shear layer regime

When the shear layer is thin $\delta \ll \lambda$, the logistic wind profile resembles Rayleigh's. As observed in the numerical analysis, the traveling trajectory is approximately 2D and remains in the neighbourhood of $z = 0$. This property greatly reduces the problem complexity and it is possible to build a quantitatively accurate analytic solution in this limit of a very thin shear layer.

The cycle may be decomposed into two parts: first, glide phases on either side of, but close to, the shear layer ($\delta \ll |z| \ll \lambda$) where the wind shear is weak and airspeed is lost due to drag, and secondly, transitions across $z = 0$ of vanishing duration but finite impulse where airspeed gain takes place.

Glide Consider the dynamics of a glider evolving according to equation (3) in the vicinity $z = 0^{\pm}$ of the separating plane but not crossing the separation layer. The 2-D approximation $z = 0^{\pm}$ brings $\gamma, \gamma' = 0$. equation (3b) becomes a constraint on the roll angle $\cos\phi = \frac{1}{c_L v^2}$ and equation (3) simplifies to

$$v' = -c_D v^2 \tag{4a}$$

$$\psi' = c_L v \sin\phi. \tag{4b}$$

Eliminating τ, the parametric evolution of v follows:

$$\frac{dv}{d\psi} = -\frac{1}{f}\frac{v}{\sqrt{1-\frac{1}{c_L^2 v^4}}} \cdot \mathrm{sign}(\psi'), \tag{5}$$

reflecting the airspeed cost of turning. The sign function is a consequence of the decrease of airspeed with time regardless of whether the turn is to port or starboard.

Layer Transition Within the thin shear layer, the wind profile can be approximated by a step function $w(z) = H(z)w_0$. The Heavyside step function $H(z)$ is 0 if $z < 0$ and 1 if $z > 0$. The time derivative of the local wind seen by the glider in equation (3e) becomes $w' = w_0\delta(z)z'$ where $\delta(z)$ is the Dirac distribution. This discontinuity in the EOM induces a finite change of the glider's state. The state transition $(\psi_-, v_-) \mapsto (\psi_+, v_+)$ can be easily computed from groundspeed continuity (a consequence of the forces remaining finite). In airspeed quantities it is expressed as $\mathbf{V}^+ = \mathbf{V}^- \pm W\mathbf{j}$ depending on whether the transition is up or down. This leads to

$$\tan\psi^+ = \tan\psi^- \pm \frac{w_0}{v^-\cos\psi^-} \tag{6a}$$

$$v^+ = v^-\sqrt{1 \pm 2w_0/v^-\sin\psi^- + (w_0/v^-)^2}. \tag{6b}$$

Note that equation (6a) is also smooth near $\psi = \pm\pi/2$. Note also that while the state (ψ^+, v^+) and (ψ^-, v^-) are taken on both sides of the shear layer, the formulas are also valid for intermediate locations within the shear layer itself. For instance, the state (ψ_0, v_0) in the middle of the shear layer $z = 0$ can be obtained from (ψ^-, v^-) (*resp.* (ψ^+, v^+)) by operating the substitution $w_0 \to w_0/2$ (*resp.* $w_0 \to -w_0/2$) in equation (6).

Cycle Periodicity Both the layer transition and the glide equation are invariant by the transformation $(w_0, \psi) \mapsto (-w_0, -\psi)$. This can be seen as the consequence of the fact that the airspeed gain of flying upwind out of the slow layer is equal to that of flying downwind into the slow layer (this symmetry is particular to the Rayleigh problem: a finite thickness shear layer or a constraint on the average travel direction would break it).

Accordingly, the physical cycle [transition up→wind layer glide→ transition down→slow layer glide] can be subdivided into two equivalent sub-units [transition→glide]→[transition→glide], expanded below:

$$\ldots(\psi^+,v^+)_{n-1}\underset{\text{glide}}{\rightarrow}\underbrace{\left[(\psi^-,v^-)_n\underset{\text{transition}}{\rightarrow}(\psi^+,v^+)_n\underset{\text{glide}}{\rightarrow}\right]}_{\text{sub-unit }n}(\psi^-,v^-)_{n+1}\ldots$$

In a stationary cycle, the airspeed is periodic $v_{n+1}=v_n$ and the heading angle is anti-periodic $\psi_{n+1}=-\psi_n$. Therefore the heading angle evolves by $\psi^-_{n+1}-\psi^+_n=\psi^-_{n+1}+\psi^+_{n+1}$ over a glide phase. The evolution of airspeed and air-relative heading angle are sketched in figure 5.

Large Glide Ratio Limit Previous studies [5] have shown that the necessary wind speed w_0 tends to 0 as the glide ratio f tends to ∞. Assuming $f\gg 1$ and $w_0\ll 1$, the loss of airspeed during the glide phase can be approximated by Euler integration

$$\Delta v_{\text{glide}}\approx -\frac{v}{f\alpha}|\Delta\psi| \text{ with } \alpha=\sqrt{1-1/c_L^2v^4} \tag{7}$$

(see ST4 for a treatment with explicit residuals). For a stationary cycle, equation (6a) used twice (between ψ^- and ψ_0 and then between ψ^+ and ψ_0) yields $\Delta\psi=\psi^++\psi^-\approx 2\psi_0$. This can be interpreted as that fact that the heading in the middle of the shear layer is approximately the average of the headings just before and just after crossing. Similarly, equation (6b), gives

$$\Delta v_{\text{transition}}=v^+-v^-\approx w_0\sin\psi_0. \tag{8}$$

When the cycle is stationary, the airspeed loss during glides and airspeed gain during transitions must compensate each other. Equating loss and gain brings the equation for the average airspeed

$$\frac{v}{\sqrt{1-1/c_L^2v^4}}=\frac{\sin\psi_0}{\psi_0}\frac{f}{2}w_0. \tag{9}$$

The minimum w_0, v pair

$$w^* = \frac{3^{3/4}\sqrt{2}}{c_L^{3/2}/c_D} \ , \quad v^* = 3^{1/4}/\sqrt{c_L} \tag{10}$$

is attained when the cardinal sine $\mathrm{sinc}(\psi_0) \equiv \sin(\psi_0)/\psi_0$ is maximized *i.e.* $\psi_0 \to 0$. The minimum wind w^* is smaller by a factor $\pi/2$, compared to when half-turns are required ($\psi_0 = \pi/2$). Note also that in the minimum-wind problem, the aerodynamic quantity of interest is the so-called coefficient of minimum power $\left(c_L^{3/2}/c_D\right)_{\max}$.

3.3 Comparison with recordings of wandering albatrosses and other numerical studies

The main characteristics of the numerical model are strikingly consistent with albatross flight data (see figures 6 and 7), and a significant improvement over the half-turn description, especially given the uncertainty associated with the wind field. In particular, Sachs' low-wind recording is both in the low-end of reports of dynamically soaring wandering albatrosses, and within 10% of the prediction of our numerical model. Turn angles are consistent ($D \geq 102$, $p \leq 10^{-20}$, see ST2) between the numerical model (65 to 100°, value for most likely conditions 80°), and Sachs' and Yonehara's albatross tracks (typically 50 to 70° in crosswind).

We also compared the model with studies based on a log-profile wind field [24, 33] and they agree within 10% for key aspects of the soaring cycle such as turn angle and required wind intensity (figures 6 and 7). This suggests that the dynamic soaring trajectory is robust to variations of the wind field, and that our 2-parameter formulation in equation (1) is successful at capturing the main characteristics of dynamic soaring, even in attached flows, *e.g.* logarithmic profiles.

4 Discussion

While in dynamic soaring the energy extraction process has historically been explained as a sequence of half-turns, high-rate GPS recordings of wandering albatrosses in crosswind flight show that they typically turn by only 50–70°, about a third of the half-turn (Figs 2*a* and 6*b*). When the shear layer being exploited for dynamic soaring is thick, as compared to the characteristic length $\lambda = \frac{2m}{\rho S}$, the minimum-wind (most energy-efficient) trajectory is indeed a succession of half-turns. When the shear layer is thin however, the minimum-wind trajectory is a succession of shallow arcs, forming a zigzagging path, as elongated as the shear layer is thin (figure 4). Similarly, our analytic model states that in thin shear layers, shallow arcs are energetically more efficient. In equation (10) and equation (12) below, we provide an analytic value for the minimum wind speed needed to sustain flight in the thin shear layer regime. As seen in figure 6, it predicts the thin shear layer limit of the numerical model and is smaller than previous studies by a factor $\pi/2$.

Wandering albatrosses exploit the shear layer just above the surface of the ocean, approximately 1 to 3 m thick. This is thin compared to $\lambda_{\text{albatross}} = 24$ m, suggesting that elongated trajectories are indeed energetically beneficial for them. For such a shear layer thickness, our numeric model predicts a turn amplitude of the minimum-wind trajectory between 65 and 100°, depending on the actual shear layer thickness and glider's aerodynamic efficiency.

In practice, several factors not taken into account in the present models may influence the cycle frequency and shape, and cause variability in the dynamic soaring trajectory. The large albatross wingspan (3 m) implies a cost of rolling not taken into account in our point-mass model, as well as a constraint on its minimum vertical travel which favour cycles of larger duration and amplitude. Waves influence the wind field through two mechanisms: wave propagation causes an updraft flow on the lee side, while wind-wave interactions influence the structure of the wind boundary layer. For instance, wind separation on the lee side of waves in a young sea state (when the wind is faster than the waves' phase speed) may result in a pocket of slow air as illustrated in figure 1a (see also [26]), with an influence on the shear layer thickness. It may be energetically beneficial for albatrosses to adapt their trajectory in order to synchronize with waves and exploit these features.

When the wind is plentiful, and the primary objective of staying aloft is easily attained, it is likely that albatrosses adapt their flight strategy in order to fulfil secondary objectives, such as choosing their beeline travel speed, reducing their overall control activity, reducing aerodynamic loads, exploring specific heights, traveling upwind, *etc.* For instance, phases when an albatross flies and remains at extreme low height without rolling may be slightly beneficial in terms of reduced drag due to ground effect; they also skew the overall beeline trajectory windward, as more time is spent in a slower flow. Overall, all these effect potentially influence the actual albatross trajectory in complex and intricate ways, and it is striking and surprising that despite changing conditions (in particular wind relative direction and intensity and wave field), the turn amplitude of crosswind flight remains relatively constant across the datasets considered.

Despite the aforementioned variability, the following conclusion holds: for the albatross, finite turns are not the cause of energy extraction, but a consequence of shear layer thickness and these other effects. The half-turn picture with up- and downwind transitions is misleading, as it is suboptimal both energetically and for travel speed.

Below, we shed additional light on the rigorous analysis of the analytic model by qualitatively discussing three intuitive explanations of the exchanges at play in the thin shear layer dynamic soaring manoeuvre.

Airspeed loss and gain Rayleigh's description of dynamic soaring, and our analytic model, both express the fact that in the thin shear layer regime, a dynamic soaring system gains airspeed each time it crosses the shear layer, and loses airspeed from drag when it flies in-between crossings. The airspeed gain upon crossing is approximately equal to the negative dot product between the wind and glider's flight direction, *i.e.* $w_0 \sin\psi_0$, as shown in equation (8). For this airspeed gain to happen (figure 2*b*,*c*), the glider must turn by an amount $\Delta\psi \approx 2\psi_0$, which is associated (see equation (7)) to an airspeed loss due to drag of $\frac{c_D}{c_L}\frac{V}{\sqrt{1-V_c^4/c_L^2V^4}}|\Delta\psi|$. As such, the airspeed loss is proportional to the angle of turn.

Therefore, while the airspeed gain during a single transition is proportional to $\sin\psi_0$, the airspeed loss is proportional ψ_0. The performance is driven by the ratio between gains and losses, which is proportional to $\sin(\psi_0)/\psi_0$, and maximized when $\psi_0 \to 0$. In the thin shear layer regime, frequent and small airspeed gains are more efficient than large and infrequent ones. This is visible in equation (9) relating airspeed, turn angle and wind intensity. Rewritten in its dimensional form (remember that $V_c = \sqrt{\frac{mg}{\frac{1}{2}\rho S}}$), it becomes

$$\frac{V}{\sqrt{1 - V_c^4/c_L^2V^4}} = \frac{\sin\psi_0}{\psi_0}\frac{c_L}{2c_D}W_0 \tag{11}$$

and the dimensional wind-airspeed relationship is

$$W^* = \frac{3^{3/4}\sqrt{2}}{c_L^{3/2}/c_D}V_c, \quad V^* = \frac{3^{1/4}}{\sqrt{c_L}}V_c. \tag{12}$$

In practice, the sensitivity of equation (11) with respect to ψ_0 is small and equation (12) approximately holds even for finite angles of turn, because the cardinal sine ($\mathrm{sinc}(\psi_0) \equiv \sin(\psi_0)/\psi_0$) is flat in the neighbourhood of 0. For instance, for 60° turns, $\mathrm{sinc}(\psi_0) = 0.95$. In fact, even quarter-turns, for which $\mathrm{sinc}(\psi_0) = 0.90$, are energetically much closer to the small turn limit $\mathrm{sinc}(0) = 1$, than to the half-turn value $\mathrm{sinc}(\psi_0) = 0.64$.

Conversely, when the shear layer is thick, the numeric analysis suggests that because crossing through it requires flying a comparatively large distance (and incurs large drag losses) anyway, maximizing the airspeed gain at each transition becomes relatively more important. Accordingly, when the shear layer is thick, the minimum-wind trajectory is composed of large-amplitude turns.

Shed vorticity and wake For a qualitative description, consider the thin shear layer case when the trajectory and flows are approximately 2D, as in the bottom of figure 2*c*. In this framework, the glider is nearly always at a large roll angle and as seen from above it resembles 2D airfoil. Successively, the glider enters a layer, performs a glide, and then leaves the layer as it transitions to the other one. Under the reasonable assumption that successive glide phases do not interact with each other, before the glider enters in a layer, the flow velocity is uniform at W_0 (wind layer) or 0 (slow boundary layer).

Because the foil generates lift, it carries bound vorticity with it. For instance in figure 2*c*, the glider is in the wind layer, and banked to starboard such that as seen from above the bound vorticity is clockwise. By Kelvin's circulation theorem, a vortex of equal intensity and opposite sign (counter-clockwise in figure 2*c*) must have been shed where the glider entered the layer. After the glide phase, the glider leaving the wind layer is a "vanishing foil" [36], and its bound vorticity is shed into the flow.

Thus, as illustrated in figure 2*c*, the effect of the glider's passage is a pair of counter-rotating vortices shed in the flow, along a generally crosswind line. These vortex pairs constitute the signature of jets, which are directed upwind in the wind layer and downwind in the slow layer. The effect of these jets is an overall slowdown of air in the fast wind layer, and acceleration of air in the slow boundary layer. In other words, through dynamic soaring the glider transfers momentum between the wind layer and the boundary layer, which tends to reduce the overall speed difference between those two layers, and is associated to the flow losing kinetic energy.

Note that the definition of kinetic energy depends on the frame of reference. In the case of crosswind dynamic soaring, it is interesting to consider the system in the inertial frame of reference convected at the average velocity between the boundary layer and the wind layer, *i.e.* $W_0/2$. In this frame, the wind layer velocity is $W_0/2$ while the boundary layer velocity is $-W_0/2$. There, both glide phases play very similar roles, with both jets tending to reduce the absolute value of the flow velocity in their respective layers. In fact, it is in this particular frame of reference that the analytic minimum wind trajectory is crosswind—it appears somehow downwind from an observer attached to earth or the water surface.

Analogy with sailing Dynamic soaring presents strong similarities to sailing: sailboats propel themselves by transferring momentum from the fast wind to the slow-moving ocean by means of two lifting surfaces, the sail and the keel. As pictured in figure 2*c* and *d*, the sail serves to extract momentum from the wind, thereby slowing it down, while the keel serves to inject that momentum to the water, thereby accelerating it. As such, the sail of a sailboat and an albatross flying in the wind layer both fulfil a “sail functionality”, while a sailboat’s keel and an albatross flying in the boundary layer both fulfil a “keel functionality”. As a consequence, the albatross can be viewed as a sequential, “flying sailboat” with the two particularities that 1) it acts between the wind layer and the boundary layer rather than between the wind and water, and 2) the sail and keel functions emerge from the dynamic soaring manoeuvre itself rather than from dedicated structural appendages as on a sailboat.

Finally, consider the sail of a sailboat, analysed in the earth frame of reference. The lift force, responsible for extracting momentum from the wind, is by definition perpendicular to the local airflow. If the sail was going directly up- or downwind, the local airflow and earth-related velocity would be aligned, the lift force and earth-related velocity would be orthogonal, and therefore the power of the lift force $\mathbf{L}.\mathbf{U}_{\text{earth}}$, would be 0. Conversely, when the sail is going crosswind, there is a misalignment between the local airflow and earth-related velocity which implies a non-zero dot product between lift and inertial velocity (a thrust force, figure 2*c*), which means extraction of power. Like the sailboat (figure 2*d*), the albatross extracts power in flight phases where it is crosswind rather than directly up- or downwind.

Conclusion

The conceptual framework presented in this paper improves the general understanding of dynamic soaring with a low-order and yet accurate model, and points to the potentially major role played by wind separation behind waves in the albatross flight. This has applications for refining the characterization and prediction of the albatross' habitat in a changing climate. In the quest for a robotic, bioinspired albatross, equation (12) may well constitute the fundamental design guideline, while understanding the key roles of shear layer thickness and turn amplitude paves the way to robust and scalable learning algorithms for online trajectory planning and control in robotic dynamic soaring applications.

Funding

This research was supported in part by a Fulbright Science and Technology fellowship, a Professor Amar G. Bose research grant, a Link Foundation Ocean Engineering & Instrumentation fellowship as well as from SMART, the Singapore-MIT Alliance for Research and Technology, within the CENSAM program.

Acknowledgements

We thank J. Izraelevitz, and L. Mendelson, as well as P. Beynet, L. Deike, A. Demarais, E. Ferenczi, J. Schulmeister, A. Teferra, A. Xibu, and the reviewers, including G. Bohrer and T. Katzner, for stimulating discussions and feedback. We also wish to acknowledge the authors of [23] and [22], namely F. Bonadonna, Y. Goto, A. P. Nesterova, G. Sachs, K. Sato, J. Traugott, Y. Watanuki, H. Weimerskirch, K. Yoda, Y. Yonehara, and L. C. Young for their enabling work in publishing the characteristics of wandering albatross flights.

Author's contributions

G.B. conceived the mechanistic model and carried the analyses. M.T. suggested the general field of study. J-J.S. supervised the study. M.T. and J-J.S. helped refine the analyses. G.B., M.T. and J-J.S. wrote the manuscript.

Competing Interests

The authors declare no competing interests.

References

1. Sachs, G. *et al.* Flying at No Mechanical Energy Cost: Disclosing the secret of Wandering Albatrosses. *PLOS one* **7** (Jan. 2012).
2. Catry, P., Phillips, R. A. & Croxall, J. P. Sustained fast travel by a gray-headed albatross (Thalassarche chrysostoma) riding an Antarctic storm. *The Auk* **121,** 1208–1213 (2004).
3. Weimerskirch, H., Guionnet, T., Martin, J., Shaffer, S. A. & Costa, D. P. Fast and fuel efficient? Optimal use of wind by flying albatrosses. *Philosophical Transactions: Biological Sciences* **267,** 1869–74 (Sept. 2000).
4. Sachs, G. & da Costa, O. *Dynamic Soaring in Altitude Region below Jet Streams* in *AIAA Guidance, Navigation, and Control Conference* (Keystone, Colorado, 2006).
5. Bower, G. *Boundary Layer Dynamic Soaring for Autonomous Aircraft: Design and Validation* PhD thesis (Stanford University, 2011).
6. Langelaan, J. W. & Roy, N. Enabling New Missions for Robotic Aircraft. *Science* **326,** 1642–1645 (2009).
7. Weimerskirch, H., Louzao, M., de Grissac, S. & Delord, K. Changes in wind pattern alter albatross distribution and life-history traits. *Science* **335,** 211–214 (2012).

8. Nevitt, G. A., Losekoot, M. & Weimerskirch, H. Evidence for olfactory search in wandering albatross, Diomedea exulans. *Proceedings of the National Academy of Sciences* **105,** 4576–4581 (Mar. 2008).
9. Rayleigh, J. W. S. The Soaring of Birds. *Nature* **27,** 534–535 (1883).
10. Richardson, P. L. How do albatrosses fly around the world without flapping their wings? *Progress in Oceanography* **88,** 46–58 (2011).
11. Jameson, W. S. *The wandering albatross* (Rupert Hart-Davis, London, 1958).
12. Cone, C. D. *A Mathematical Analysis of the Dynamic Soaring Flight of the Albatross with Ecological Interpretations* tech. rep. (1964), 1–104.
13. Wood, C. J. The flight of albatrosses (a computer simulation). *Ibis* **115** (1973).
14. Boslough, M. B. E. *Autonomous Dynamic Soaring Platform for Distributed Mobile Sensor Arrays* tech. rep. (Sandia National Laboratories, 2002).
15. Lissaman, P. *Wind Energy Extraction by Birds and Flight Vehicles* in *AIAA Guidance, Navigation, and Control Conference* (Reno, Nevada, 2005).
16. Barate, R., Doncieux, S. & Meyer, J.-A. Design of a bio-inspired controller for dynamic soaring in a simulated unmanned aerial vehicle. *Bioinspiration & biomimetics* **1,** 76–88 (2006).
17. Denny, M. Dynamic soaring: aerodynamics for albatrosses. *European Journal of Physics* **30,** 75–84 (Jan. 2009).

18. Lawrance, N. R. J. *Autonomous Soaring Flight for Unmanned Aerial Vehicles* PhD thesis (University of Sidney, 2011).

19. Bonnin, V. & Toomer, C. C. *Energy-Harvesting Mechanisms for UAV Flight by Dynamic Soaring* in *AIAA Guidance, Navigation, and Control Conference* (Boston, MA, 2013).

20. Bird, J. J., Langelaan, J. W., Montella, C., Spletzer, J. R. & Grenestedt, J. L. *Closing the Loop in Dynamic Soaring* in *AIAA Guidance, Navigation, and Control Conference* (National Harbor, Maryland, 2014).

21. Gao, X.-Z., Hou, Z.-X., Guo, Z. & Chen, X.-Q. Energy extraction from wind shear: Reviews of dynamic soaring. *Proceedings of the Institution of Mechanical Engineers, Part G: Journal of Aerospace Engineering* **229,** 2336–2348 (2015).

22. Sachs, G., Traugott, J., Nesterova, A. P. & Bonadonna, F. Experimental verification of dynamic soaring in albatrosses. *The Journal of experimental biology* **216,** 4222–32 (Nov. 2013).

23. Yonehara, Y. *et al.* Data from: Flight paths of seabirds soaring over the ocean surface enable measurement of fine-scale wind speed and direction. *Dryad, doi:10.5061/dryad.3pb86* (2016).

24. Flanzer, T. C., Bunge, R. A. & Kroo, I. M. *Efficient Six Degree of Freedom Aircraft Trajectory Optimization with Application to Dynamic Soaring* in *AIAA Aviation Technology, Integration, and Operations Conference* (Indianapolis, Indiana, 2012).

25. Deittert, M., Richards, A., Toomer, C. A. & Pipe, A. Engineless Unmanned Aerial Vehicle Propulsion by Dynamic Soaring. *Journal of Guidance, Control, and Dynamics* **32,** 1446–1457 (Sept. 2009).
26. Buckley, M. P. & Veron, F. Structure of the Airflow above Surface Waves. *Journal of Physical Oceanography* **46,** 1377–1397 (2016).
27. Pennycuick, C. J. Gust soaring as a basis for the flight of petrels and albatrosses (Procellariiformes). *Avian Science* **2,** 1–12 (2002).
28. Pennycuick, C. J. *Modelling the flying bird* (Elsevier, 2008).
29. Phillips, W. H. Propulsive Effects due to Flight through Turbulence. *Journal of Aircraft* **12,** 624–626 (1975).
30. Patel, C. K., Lee, H.-T. & Kroo, I. M. *Extracting Energy from Atmospheric Turbulence* in *XXIX OSTIV Congress* (Lüsse-Berlin, Germany, 2008).
31. Zhao, Y. J. Optimal patterns of glider dynamic soaring. *Optimal control applications and methods* **25,** 67–89 (2004).
32. Pennycuick, C. J. The Flight of Petrels and Albatrosses (Procellariiformes), Observed in South Georgia and its Vicinity. *Philosophical Transactions: Biological Sciences* **300,** 75–106 (1982).
33. Sachs, G. Minimaler Windbedarf für den dynamischen Segelflug der Albatrosse. *Journal für Ornithologie* **134,** 435–445 (1993).

Mass m (kg)	9.5
Wing area S (m^2)	0.65
Minimum power coefficient $\left(c_L^{3/2}/c_D\right)_{\max}$	22
λ (m)	24.3
V_c (m/s)	15.5

Table 1: Characteristics of the albatross used in this study. λ and V_c are calculated with the air density $\rho = 1.2\ \mathrm{kg/m^3}$ and acceleration of gravity $g = 9.8\ \mathrm{m/s^2}$.

34. Gent, P. R. & Taylor, P. A. A note on 'separation' over short wind waves. *Boundary-Layer Meteorology* **11,** 65–87 (1977).

35. Yonehara, Y. *et al.* Flight paths of seabirds soaring over the ocean surface enable measurement of fine-scale wind speed and direction. *Proceedings of the National Academy of Sciences of the United States of America* **113,** 9039–9044 (2016).

36. Steele, S. C., Dahl, J. M., Weymouth, G. D. & Triantafyllou, M. S. Shape of retracting foils that model morphing bodies controls shed energy and wake structure. *Journal of Fluid Mechanics* **805,** 355–383 (2016).

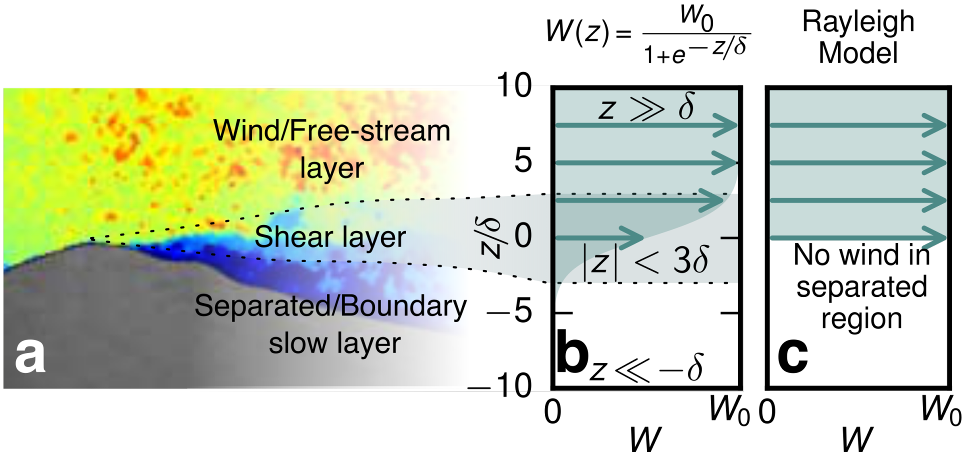

Figure 1: **Wind profile**. (**a**) Wind field behind waves. Colour-coding: wind intensity, experimental data adapted from [26]. (**b**) The logistic wind profile in this study captures adequately the wind field in separated regions, such as behind ocean waves. More generally, it constitutes a robust way to approximate a wide class of wind fields, based on two parameters: a typical wind speed inhomogeneity W_0 separated by a shear layer of typical length-scale δ. (**c**) Rayleigh's wind model is the limit of the logistic profile for $\delta \to 0$.

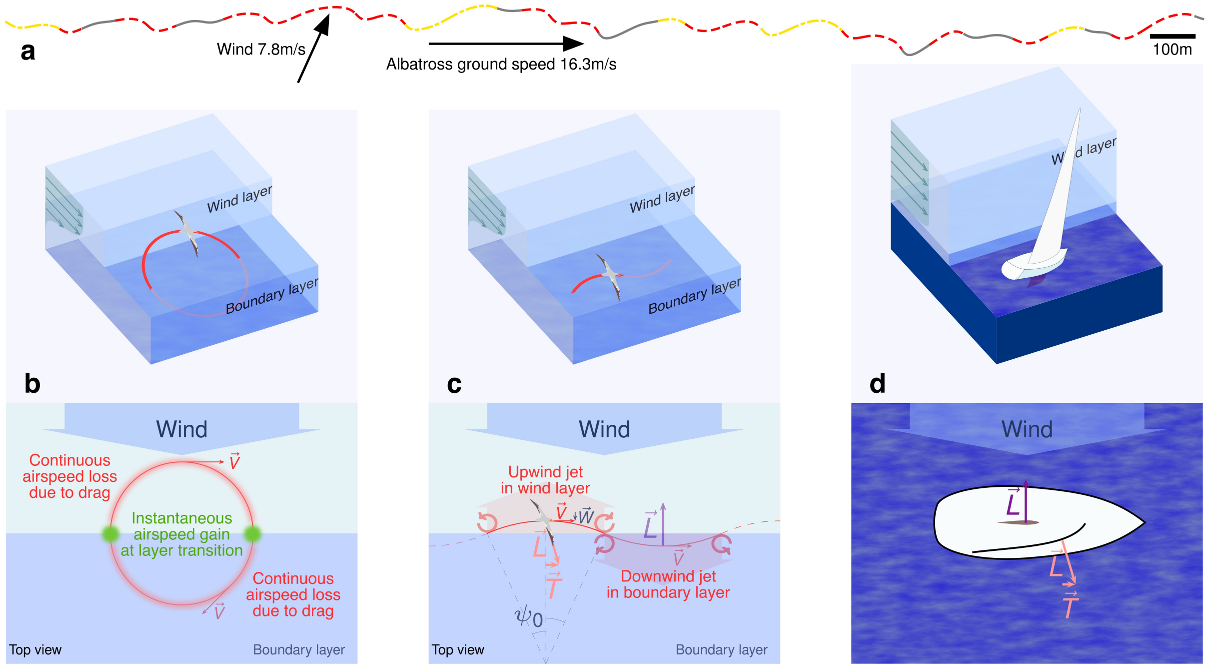

Figure 2: **The albatross' trajectory**. (**a**) Recording of a flying albatross from [22] (top view). In crosswind flight the typical turn of the albatross is about 50–70°. Dot-dashed yellow portions of the trajectory: the albatross is involved in a 60° turn within ±20°. Dashed red portions: the albatross is involved in a 60° turn within ±10°. Note that while in the ground frame the mean albatross travel has a downwind component, in the frame moving with the average wind it is nearly crosswind. (**b**) The Rayleigh cycle describes the albatross' flight as a sequence of half-turns between the windy and slow regions. At each layer transition, there is an airspeed gain equal to the wind speed, which compensates inherent drag losses that are quadratic in airspeed. However this trajectory is suboptimal for energy extraction. Instead, for thin shear layers, the optimal cycle (**c**) is composed of a succession of small-angle arcs. The flight portion in the wind layer is functionally analogous to the sail of a sailboat, while the portion in the slow layer is analogous to the keel of a sailboat (**d**).

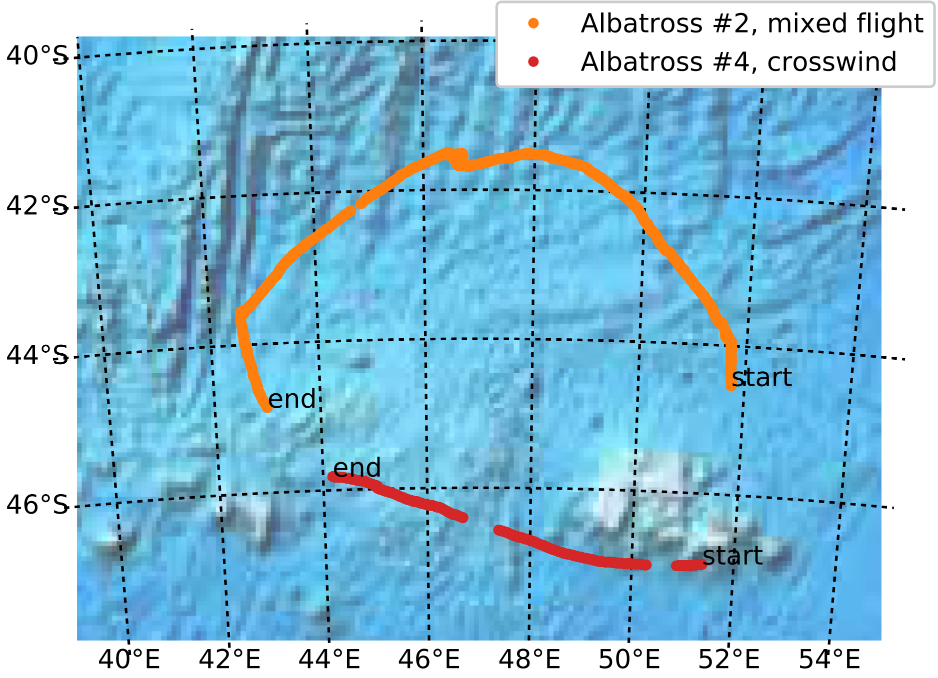

Figure 3: **Wandering albatrosses** #2 and #4 from Yonehara *et al.* [23], analysed in this study. The track of albatross #2 is over 1,700-kilometre-long, lasts for approximately two days and is made of up-, cross- and downwind flights in low and high winds, separated by active foraging and resting periods. The track of albatross #4 is a nearly uninterrupted, 650-kilometre, 9-hour, approximately crosswind flight performed in 8–15 m/s winds. Note that some data is missing or dropped due to poor GPS quality.

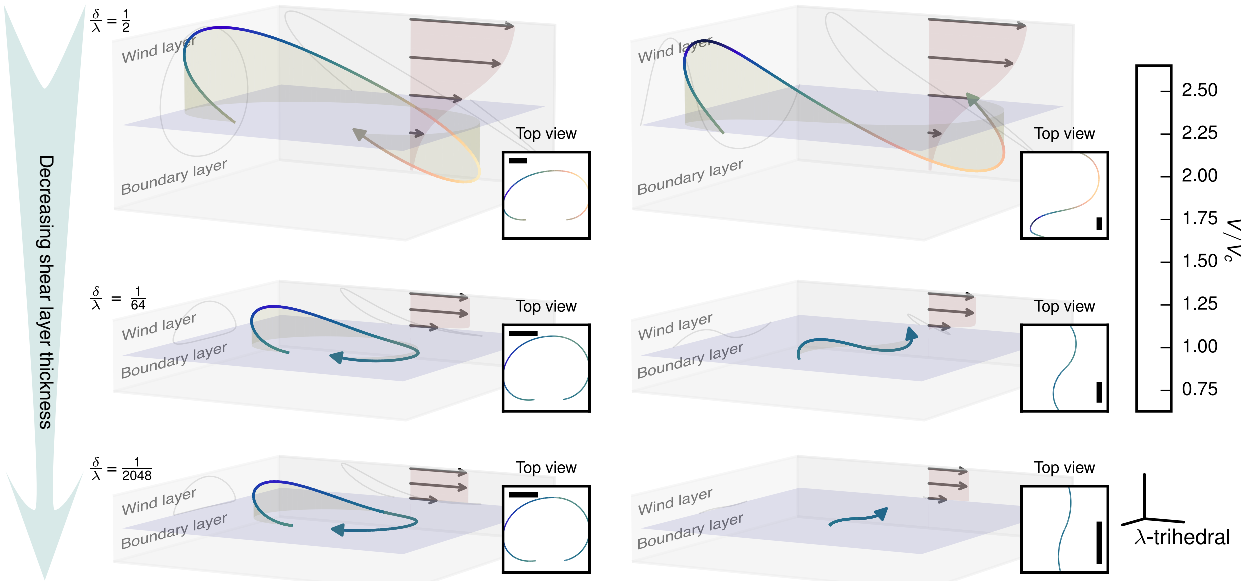

Figure 4: **Minimum wind trajectories** for three shear layer thicknesses (see the wind profiles in the plots' backgrounds and how they relate to shear layer thickness in figure 1). On the left, the trajectories are constrained to fulfil the specific requirement that the heading increases by 360° over a cycle, hence their loitering appearance. On the right, the heading is required to be periodic, hence their traveling appearance. For the 3D trajectory the scale is common and is indicated on the bottom right corner: the trihedral is of length $\lambda = \frac{2m}{\rho S}$ (24 m for an albatross). Similarly, the scale bars on the top views are of length λ. The middle plots $\delta/\lambda = 1/64$ are representative of the shear layer thickness experienced by albatrosses. The traveling trajectory requires less wind than the loitering one, with an increasing advantage for thinner shear layers. When $\delta/\lambda \to 0$, the traveling trajectory becomes 2D and is composed of a sequence of vanishingly small arcs of finite curvature performed at nearly constant speed. The behaviour of the loitering trajectory is qualitatively different: for decreasing shear layer thicknesses, it quickly converges to a limit trajectory that remains significantly 3D even for an infinitely thin shear layer.

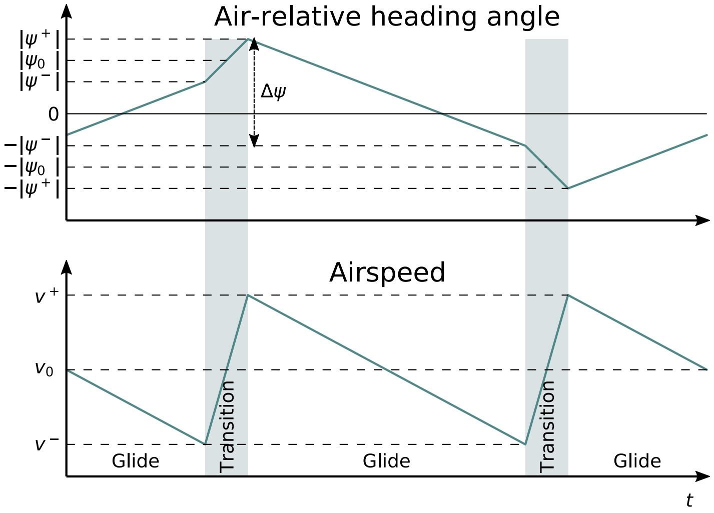

Figure 5: **Sketch of the evolution of airspeed and air-relative heading angle** over one dynamic soaring cycle, in the large glide ratio approximation. Following a glide phase in the boundary layer, the glider transitions into the wind layer, experiencing a shift of its air-related heading to port, as well as an airspeed boost. A glide phase in the wind layer ensues and is followed by a transition into the boundary layer which is associated to a shift of air-related heading to starboard and an airspeed boost. The cycle in this figure starts 1/4 period earlier than in the right-hand side of figure 4. In the thin shear layer limit, airspeed has double periodicity and air-related heading has double anti-periodicity, such that the physical cycle may be divided into two equivalent sub-units.

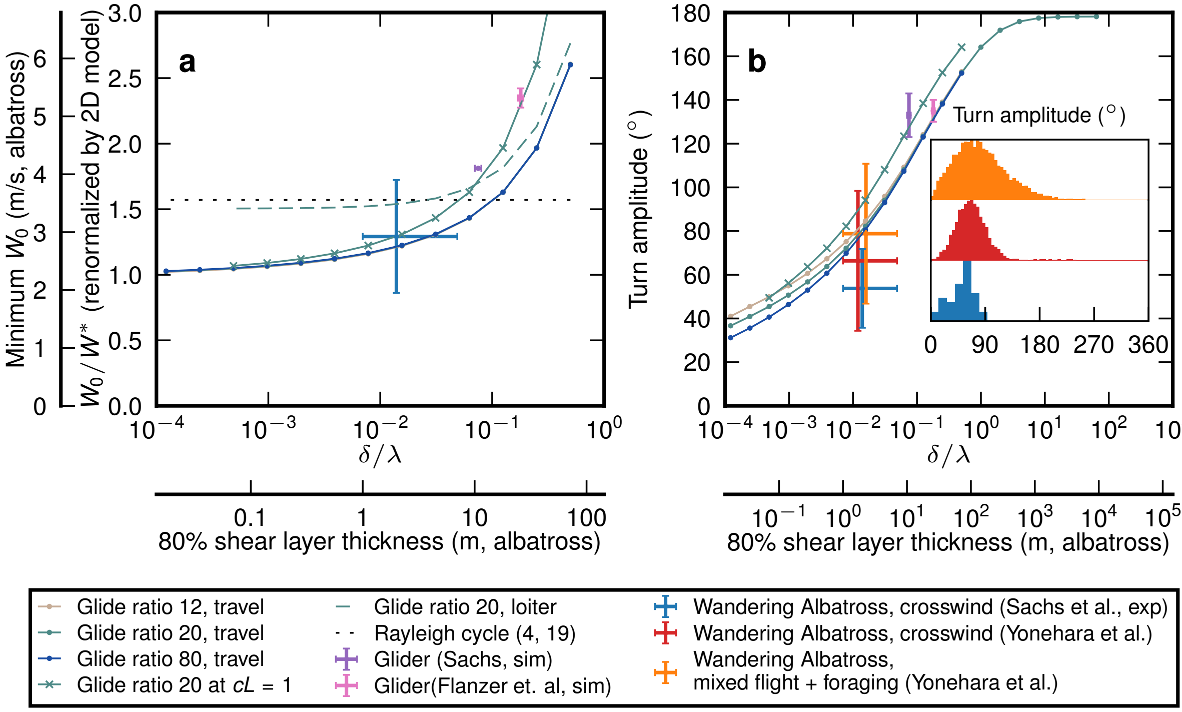

Figure 6: **Minimum wind and turn amplitude** of the traveling and loitering trajectories as a function of the shear layer thickness from our numerical model, for various glide ratios. Unless otherwise indicated, the maximum glide ratio is reached at $c_L = 0.5$. The model is compared with experimental data of flying albatrosses from [22, 23], and simulations of dynamic soaring in a logarithmic wind field from [24, 33]. (**a**) In the thin shear layer regime $\delta \to 0$ the wind required for the traveling trajectories converges to our 2D model in equation (12). (**b**) Similarly, the turn amplitude decreases and the trajectories become straighter. The histogram insets represent the turning statistics of Sachs *et al.* [22], Yonehara *et al.* [23] albatross #4 and #2 from bottom to top. Yonehara's albatrosses are recorded over hundreds of kilometres. In crosswind the recorded albatrosses typically turn by 50–70° while in the recorded mixed-flight the typical turn amplitude is 80°. Error bars represent the median turn ± 1 std.

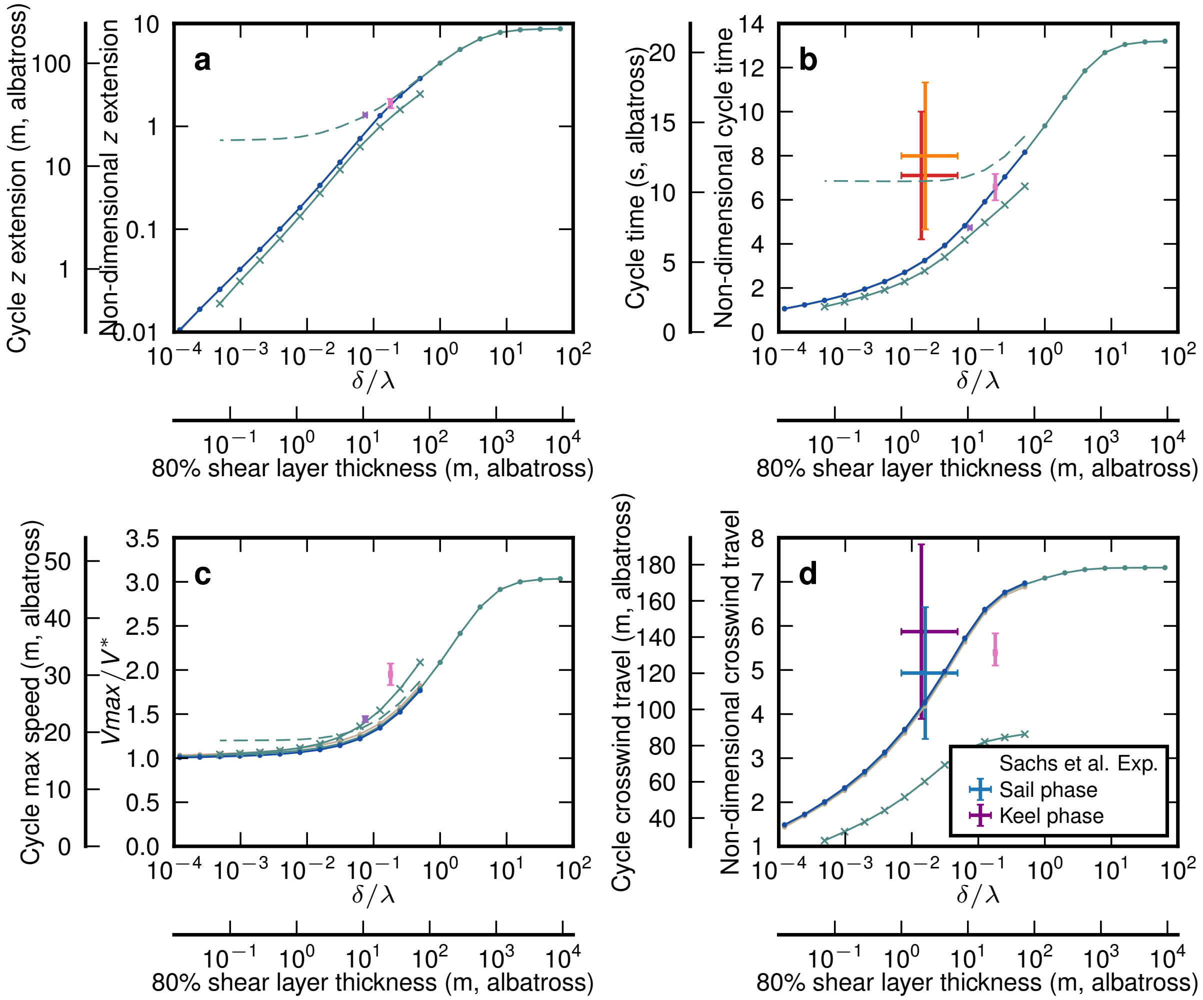

Figure 7: **Characteristics of the minimum-wind cycle**. Same legend as in figure 6. (**a**) Height separation between the lowest and highest point of the cycle. For thin shear layers the traveling trajectory is nearly 2D. Note that the convergence rate is only about $z \sim \delta^{2/3}$. (**b**) Cycle duration. (**c**) Maximum airspeed attained during the cycle. (**d**) Crosswind travel during one cycle. The orange (*resp.* purple) dots correspond to twice the length of the sail (*resp.* keel) phase in figure 2*a*.

Journal of the Royal Society Interface
Supplementary information for

Optimal dynamic soaring consists of successive shallow arcs

Gabriel D. Bousquet[1], Michael S. Triantafyllou, Jean-Jacques E. Slotine
Department of Mechanical Engineering, Massachusetts Institute of Technology,
Cambridge, MA, 02139, USA

ST1 Numerical solution by direct collocation

Numerical procedure

Our numerical model for figures 4 to 7 is based on the EOM of equation (3) with $w(z) = \frac{w_0}{1+\exp -z/\delta}$. We formally rewrite the EOM $\dot{\mathbf{x}} = f(\mathbf{x}, \mathbf{u})$. The question that we want answered is the following: *For a given glider* ($c_{D,0}, f_{\max}$) *and a given shear layer thickness* δ*, what is the minimum wind speed inhomogeneity parameter* w_0 *that has feasible trajectories, periodic in the state* $\mathbf{x}$*?* More specifically, for the traveling trajectories (right-hand side of figure 4 and figure 6), the boundary conditions are $V(T) = V(0), \psi(T) = \psi(0), \gamma(T) = \gamma(0), z(T) = z(0)$. For the circular trajectories (left-hand side of figure 4, we imposed the boundary conditions $V(T) = V(0), \psi(T) = \psi(0) + 2\pi, \gamma(T) = \gamma(0), z(T) = z(0), x(T) = x(0)$. Note that the x-constraint in the latter set of boundary conditions is not strictly required. Without it the upper half cycle tends to peak at a higher altitude, with very small airspeed and very large c_L. The x-constraint maintains c_L to realistic values while conserving the main features of the unconstrained trajectories.

The question is cast into a finite dimensional optimization problem by direct collocation. First, time over one period T is discretized into time steps $[0, n_1T, n_2T, \dots, n_{N-1}T, T]$ with $0 < n_1 < \cdots < n_{N-1} < 1$. The spacing need not be uniform. We use the shorthand $\mathbf{x}_i \hat{=} \mathbf{x}(n_iT), \mathbf{u}_i = \mathbf{u}(n_iT)$. Following *e.g.* [24, 37], the continuous-time constraints $\mathbf{x}(n_iT) = \int_{n_{i-1}T}^{n_iT} f(\mathbf{x}(t), \mathbf{u}(t))dt$ are approximated by

$$\begin{aligned}
\mathbf{u}_{m_i} &= \frac{1}{2}(\mathbf{u}_i + \mathbf{u}_{i-1}) \\
\mathbf{x}_{m_i} &= \frac{1}{2}(\mathbf{x}_i + \mathbf{x}_{i-1}) - \frac{1}{8}(f(\mathbf{x}_i, \mathbf{u}_i) - f(\mathbf{x}_{i-1}, \mathbf{u}_{i-1}))(n_i - n_{i-1})T \\
0 = \mathbf{C}_i &= \mathbf{x}_{i-1} + \frac{1}{6}\left(f(\mathbf{x}_i, \mathbf{u}_i) + 4f(\mathbf{x}_{m_i}, \mathbf{u}_{m_i}) + f(\mathbf{x}_{i-1}, \mathbf{u}_{i-1})\right)(n_i - n_{i-1})T
\end{aligned}$$

---

[1] `g_b@mit.edu`

For the traveling problem, the previous discretization leads to the following nonlinear program (NLP):

$$\begin{aligned}
\underset{\mathbf{x}_0,\ldots,\mathbf{x}_N,\mathbf{u}_0,\ldots,\mathbf{u}_N,w_0,T}{\text{minimize}} \quad & w_0 \\
\text{subject to} \quad & \mathbf{C}_i = 0, \quad i = 1, \ldots, N \\
& (V_N, \psi_N, \gamma_N, z_N) = (V_0, \psi_0, \gamma_0, z_0) \\
\text{and} \quad & z_0 = 0 \\
& V_i, c_{L,i} > 0 \\
& -\pi < \psi_i < \pi, \ -\pi/2 < \gamma_i < \pi/2
\end{aligned} \tag{13}$$

A solution to the NLP is a feasible trajectory that locally minimizes the wind required for flight. Note that the last three relations are purely technical and the inequalities constraints were not active upon solution convergence.

Similarly, the circular problem is cast into

$$\begin{aligned}
\underset{\mathbf{x}_0,\ldots,\mathbf{x}_N,\mathbf{u}_0,\ldots,\mathbf{u}_N,w_0,T}{\text{minimize}} \quad & w_0 \\
\text{subject to} \quad & \mathbf{C}_i = 0, \quad i = 1, \ldots, N \\
& (V_N, \psi_N, \gamma_N, z_N, x_N) = (V_0, \psi_0 + 2\pi, \gamma_0, z_0, x_0) \\
\text{and} \quad & z_0 = 0 \\
& V_i, c_{L,i} > 0 \\
& -3\pi < \psi_i < 3\pi, \ -\pi/2 < \gamma_i < \pi/2
\end{aligned} \tag{14}$$

The problem was then solved for various $(c_{D,0}, f_{\max}, \delta)$ with a nonlinear solver *e.g.* SNOPT. We typically used $N = 140$ time steps, leading to $O(1000)$ variables and constraints. Our Python implementation converged in $O(1-10)$ minutes on a 2013 Macbook Pro. We used more time steps than in similar studies. The main reason for this choice is that for small δ the transition through the shear layer is of short duration, and resolving it requires a high level or granularity. To reach very small values of δ and validate the convergence of our numerical model to our analytic model, we leveraged on the possibility to utilize non-uniform time spacing: we started by solving problems with large δ and subsequently addressed smaller δ by adaptively refining the time spacing near the transition in order to maintain a sufficient resolution.

Results

The raw results for the cases illustrated in figure 4 are collected in figures S2–S4 and S5–S7 and their characteristics are displayed in figures 6 and 7. For case with $\delta = 1/64$ and $1/2048$, the control points are non-uniformly spaced and are denser near the transition $z = 0$. For both the circular and traveling cases, $\delta = 1/64$ and $1/2048$ are qualitatively

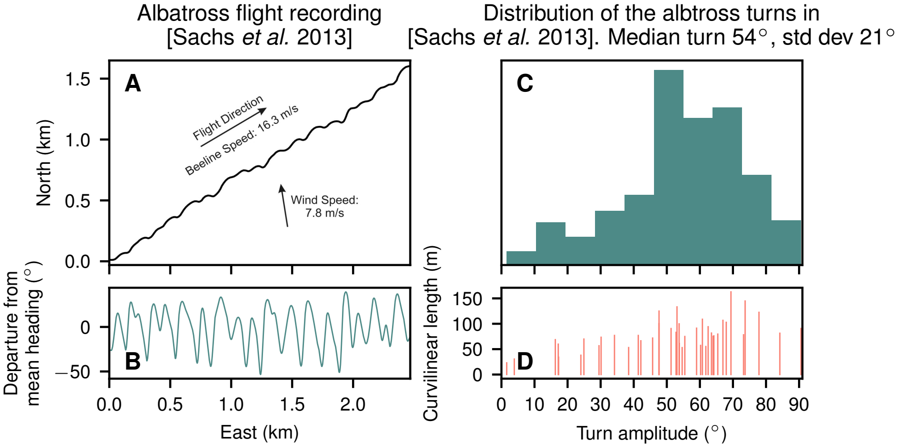

Figure S1: **Analysis of the albatross' trajectory**. (**a**) Recording of an albatross travelling across a low wind [22]. (**b**) Albatross heading along the trajectory. In (**c**) the statistical analysis of the flight shows that the albatross' median turns is 54° (mean 50°). In this particular recording, the albatross virtually never turns more than 90°. (**d**) Curvilinear length of the individual turns.

similar. The boundary thickness for the albatross is closest to case $\delta = 1/64$. For the traveling cases $\delta = 1/64$ and $1/2048$, the sub-periodicity discussed in section 3.2 is visible—a qualitative difference from $\delta = 2$. In contrast, all circular cases are qualitatively similar to each other across the range of δ's.

Figures S8–S11 show the minimum-wind trajectories in a wind field of the form $W(z) = W_0\left(2 + \frac{1}{1+\exp -z/\delta}\right)$. In those cases, the aerodynamic quantities are unchanged, but the overall trajectory is convected at an additional speed $2W_0$. This models instances where the glider may access a boundary layer where the wind is only partially slowed down, as is the case in practice.

ST2 GPS data analysis

Sachs *et al.* recordings

The data for figures 2 and 6 were extracted from the bitmap figure 9A of [22] (reproduced in figure S1a). For each pixel in the East direction, the centre of the trajectory line was determined by an average operation. The result was filtered with the `filtfilt` filter from `scipy.signal`. The (ground) heading angle was then calculated (figure S1b). Figure S1c,d reports the distribution of the turns in the recording.

Yonehara *et al.* recordings

Yohehara *et al.* [23] contain latitude–longitude time histories of wandering albatrosses (*Diomedea exulans*). The tracks are sampled at 1 Hz and for the tracks of interest in the present study (albatrosses 1 and 4), the recording is about 48h long, with periods of flight, foraging, and rest on water.

The latitude–longitude data is first converted to distances by projection with Python's `Basemap` cylindrical equidistant projection centred at (47° East, 43° South). The trajectory is then interpolated at 5 Hz with a cubic spline using Python's `interp1d`. Each point is attributed a heading angle by centred finite difference of the positions at 5 Hz. A search for local extrema is performed on the unwrapped heading angle. Because the cubic spline introduces some oscillation in the trajectory in some places, if local maxima and minima follow each other by less than 2.5 s, they are merged together and replaced by a single point of average heading. This technique was chosen over linear interpolation or filtering as both reduce peaks in heading angles and would underestimate the amplitude of turns. The obtained time history of local minima and maxima of heading angle were used to obtain the sequence of turn amplitudes.

The data points when the groundspeed was outside the 5–50 m/s range were removed, as they tend to represent either phases where the albatross is resting on water, or unrealistic GPS recordings. We also set aside the turns of amplitude greater than 360° which are concentrated within periods of active foraging (they account for about 1% of the turns).

For albatross #4, a further step was taken. We started with the long westward flight of Albatross #4 (approximately 650 km on March 18, 2007 from 6:02AM to 4:37PM). Along the travel sequence, there are a few instances where the albatross seemed to be foraging (not making progress for significant stretches of time), or when the GPS recording was spotty (unrealistic and sporadic jumps in the data). For this reason, we removed 5 time intervals, varying in duration from 2 to 47 min, for a total of 1h47. The resulting tracks are shown in figure 3.

Empirical Analysis

The sample standard deviation is 21° and 32° for Sachs' albatross and Yonehara's albatross #4, respectively. With 40 and 3,680 samples respectively, within the approximation of the central limit theorem, the standard deviation of the sample mean pdf is 3.3 and 0.5°, respectively.

Our numerical model predicts a typical turn angle of 80°. Compared to the half-turn description (null hypothesis), the log-likelihood ratio based on the *t*-test pdf is 102 for Sachs' albatross ($p < 10^{-23}$) and $4 \cdot 10^4$ for Yonehara's albatross #4 ($p < 10^{-300}$). In view of the data from albatross #4, the prediction of our numerical model is 10^{8700} times more likely than the half-turn's.

ST3 Comparison with log-based numerical approaches

In figures 6 and 7, we compare our models with existing numerical literature in a log profiles. [33] was chosen because it is the first full trajectory optimization in a log field (precisely, a power law) in our knowledge. It is also used as a validation case in [25]. [24] compares 3 DoF, 6 DoF, and panel-based aircraft models and is a the most complete study, in our knowledge, of the sensitivity of the minimum-wind trajectory in a log profile, therefore constituting a reference for assessing relative significance of mismatches and sensitivities.

Both references consider the minimum-wind trajectory in a log (or power law) wind profile, and set a minimum authorized minimum altitude (or wing-tip clearance from the water). In order to compare with our own model and extract an equivalent shear layer, we measured on in both cases the thickness $\Delta_{80\%}$ such that

$$\frac{W(z_{\min} + \Delta_{80\%}) - W(z_{\min})}{W(20\text{m}) - W(z_{\min})} = 80\%$$

and converted that value back into the non-dimensional shear layer parameter δ. Overall, the quantities used for comparison are collected in Table S1.

While both studies attempt to model a glider over a similar hypothetical shear layer above the ocean surface, they lead to a somewhat different shear layer parameter δ because the wing-loadings considered are different. Overall, despite model differences (for instance, our model does not enforce a maximum lift coefficient), the results all agree well with each other. In particular, the sensitivity of the minimum-wind trajectory with respect to the wind parameterization, whether logarithmic, or modelled with a logistic function, is small, validating our approach.

Finally, as also mentioned in the article, the natural frame of reference in which to analyse the minimum-wind problem is the frame convected with the average wind (for instance approximately $w(z=0)$ in our model, or $(W(z_{\min})+W(z_{\max}))/2$ in a log profile). There, the problem's symmetry is maximized and the trajectory is simplified. Within their respective models, [24, 33] underline the fact that because the glider is forbidden to reach the no-wind region which is confined to the very surface, only 25–35% of the range of wind may in fact be accessed. In our model, this could modelled by considering the wind profile

$$W(z) = W_0 \left(n + \frac{1}{1 + \exp -z/\delta} \right)$$

where $n \approx 2 - 3$ is some multiplicative factor reflecting that the wind speed in the lower layer is non-zero. Equivalently, this amounts to considering that the trajectory is convected downstream at an additional rate nW_0. The trajectories in this configuration are represented in figures S8–S11. Note that the trajectory in S8 is extremely similar to that in [33], for a similar shear layer thickness. Likewise, the trajectory in figure S11 (and previous figures) is similar to that of the albatross in figure 2, suggesting again the probable ability of the albatross to reach the slow and separated regions behind waves. Statistical analysis of the albatross' height during dynamic soaring would help validate and/or refine this hypothesis.

ST4 Complements on the thin shear layer regime analytic model

In the thin shear layer limit, let ψ_0 and v_0 be the air-relative heading and speeds at altitude $z = 0$ *i.e.* centred in the middle of the shear layer. Define $\bar{\psi} = (\psi^+ + \psi^-)/2$, $\bar{v} = (v^+ + v^-)/2$ and $\Delta v = v^+ - v^-$. Assume periodic (energy neutral) conditions. If f and c_L are kept constant, the evolution of airspeed during glide in equation (5) can be rewritten as

$$\int_{v_+}^{v^-} \sqrt{1 - \frac{1}{c_L^2 v^4}} \frac{dv}{v} = -\frac{1}{f} \int_{\psi_n^+}^{\psi_{n+1}^-} d\psi. \tag{15}$$

Integrate the left-hand side with the third order accurate midpoint approximation at $\bar{v}$. Integrate the right-hand side and recall that due to the antisymmetry of the equations, the turn amplitude of the glide phase is $2\bar{\psi}$. This gives

$$\sqrt{1 - \frac{1}{c_L^2 \bar{v}^4}} \frac{\Delta v}{\bar{v}} + O(\Delta v^3) = \frac{2}{f} \bar{\psi}. \tag{16}$$

The relations of transition for the heading are:

$$\begin{aligned} \tan \psi^+ &= \tan \psi_0 + \frac{w_0}{2 v_0 \cos \psi_0} \\ \tan \psi^- &= \tan \psi_0 - \frac{w_0}{2 v_0 \cos \psi_0}. \end{aligned} \tag{17}$$

The relations of transition for the airspeed are

$$\begin{aligned} v^+ &= v_0 \sqrt{1 + \frac{w_0}{v_0} \sin \psi_0 + \left(\frac{w_0}{2 v_0}\right)^2} \\ v^- &= v_0 \sqrt{1 - \frac{w_0}{v_0} \sin \psi_0 + \left(\frac{w_0}{2 v_0}\right)^2}. \end{aligned} \tag{18}$$

The following Taylor expansions follow:

$$\bar{\psi} = \psi_0 + O\left(\left(\frac{w_0}{v_0 \cos\psi_0}\right)^2\right) \tag{19a}$$

$$\bar{v} = v_0 \left\{1 + O\left(\left(\frac{w_0}{v_0}\right)^2\right)\right\} \tag{19b}$$

$$\Delta v_{\text{transition}} = w_0 \sin\psi_0 + O\left(\frac{w_0^3}{v_0^2}\right). \tag{19c}$$

Below we assume that v_0, ψ_0 are fixed, and express the residuals in terms of w_0. The residual in equation (16) can now be transformed with equation (19c) to $\Delta v = O(w_0)$, and the quantities $\bar{\psi}$ and $\bar{v}$ can be replaced with ψ_0 and v_0 at the price of a $O(w_0^2)$ error. The equation of glide becomes

$$\alpha_0 \frac{\Delta v}{v_0} = \frac{2}{f}\psi_0 + O(w_0^2)$$

with $\alpha_0 = \sqrt{1 - \frac{1}{c_L^2 v_0^4}}$. This is equation (7) where the approximation is exhibited. Combining it with the equation of transition (19c), the balance between airspeed gains and losses is

$$\alpha_0 \frac{w_0 \sin\psi_0}{v_0} = \frac{2}{f}\psi_0 + O(w_0^2)$$

which is similar to equation (9). Note that for any triplet (v_0, w_0, ψ_0) such that equation (15) is integrable, and $\bar{\psi}$ is not strictly 0, the equation has a solution if f can be chosen arbitrarily.

For any given fixed ψ_0, v_0, now decrease w_0 (equivalently, increase f). The residual in w_0^2 is dominated and the equation converges to

$$\frac{v_0}{\alpha_0} = \frac{\sin\psi_0}{\psi_0}\frac{f}{2}w_0 \tag{20}$$

i.e. equation (9).

References

22. Sachs, G., Traugott, J., Nesterova, A. P. & Bonadonna, F. Experimental verification of dynamic soaring in albatrosses. *The Journal of experimental biology* **216,** 4222–32 (Nov. 2013).

23. Yonehara, Y. *et al.* Data from: Flight paths of seabirds soaring over the ocean surface enable measurement of fine-scale wind speed and direction. *Dryad, doi:10.5061/dryad.3pb86* (2016).

	Sachs 1993 [33]	Flanzer 2012 [24]
V_c (m/s)	14.9	8.2
$\left(c_L^{3/2}/c_D\right)_{\max}$	24.2	19.4
W^* (m/s)	3.8	3.2 ± 0.1
δ (non-dim.)	0.075 ± 0.05	0.18 ± 0.01
$\Delta_{80\%}$ (m)	10	7.3
$z_{\max} - z_{\min}$ (m)	19.2	11.5
$V_{\max}$ (m/s)	21.5 ± 0.5	16 ± 1
t^* (s)	7.2	5.5 ± 0.5

Table S1: **Minimum-wind trajectory in a logarithmic wind** as reported by [24, 33]. $(z_{\max} - z_{\min})$ represents the distance between the maximum and minimum altitudes reached by the glider over one cycle. Note that also the physical boundary layer thickness is comparable in both studies, because of a smaller wing loading, upon non-dimensionalisation is appear thicker in [24].

24. Flanzer, T. C., Bunge, R. A. & Kroo, I. M. *Efficient Six Degree of Freedom Aircraft Trajectory Optimization with Application to Dynamic Soaring* in *AIAA Aviation Technology, Integration, and Operations Conference* (Indianapolis, Indiana, 2012).

25. Deittert, M., Richards, A., Toomer, C. A. & Pipe, A. Engineless Unmanned Aerial Vehicle Propulsion by Dynamic Soaring. *Journal of Guidance, Control, and Dynamics* **32,** 1446–1457 (Sept. 2009).

33. Sachs, G. Minimaler Windbedarf für den dynamischen Segelflug der Albatrosse. *Journal für Ornithologie* **134,** 435–445 (1993).

37. Hargraves, C. R. & Paris, S. W. Direct Trajectory Optimization Using Nonlinear Programming and Collocation. *AIAA J. Guidance* **10,** 338–342 (1987).

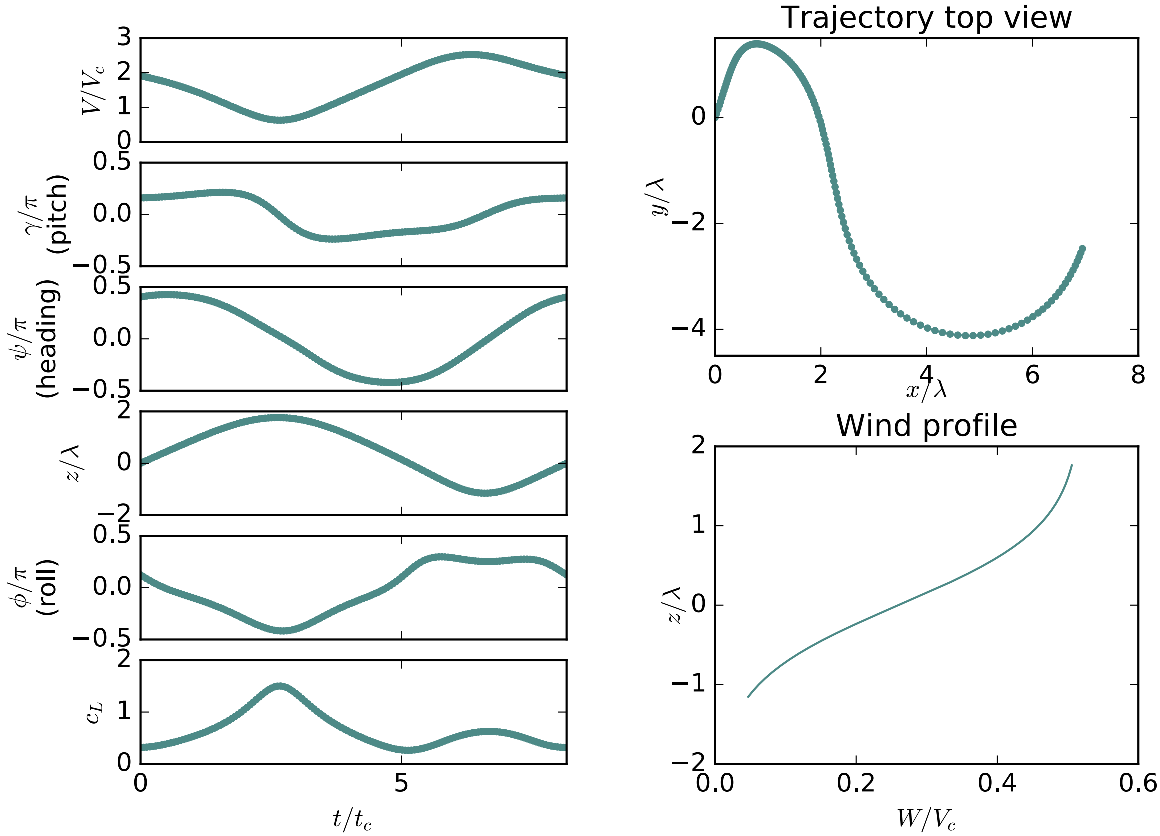

Figure S2: **Solution to the Rayleigh problem** for $f_{\max} = 20, c_{L,f_{\max}} = 0.5, \delta = \lambda/2$. $w_0 = 0.52$.

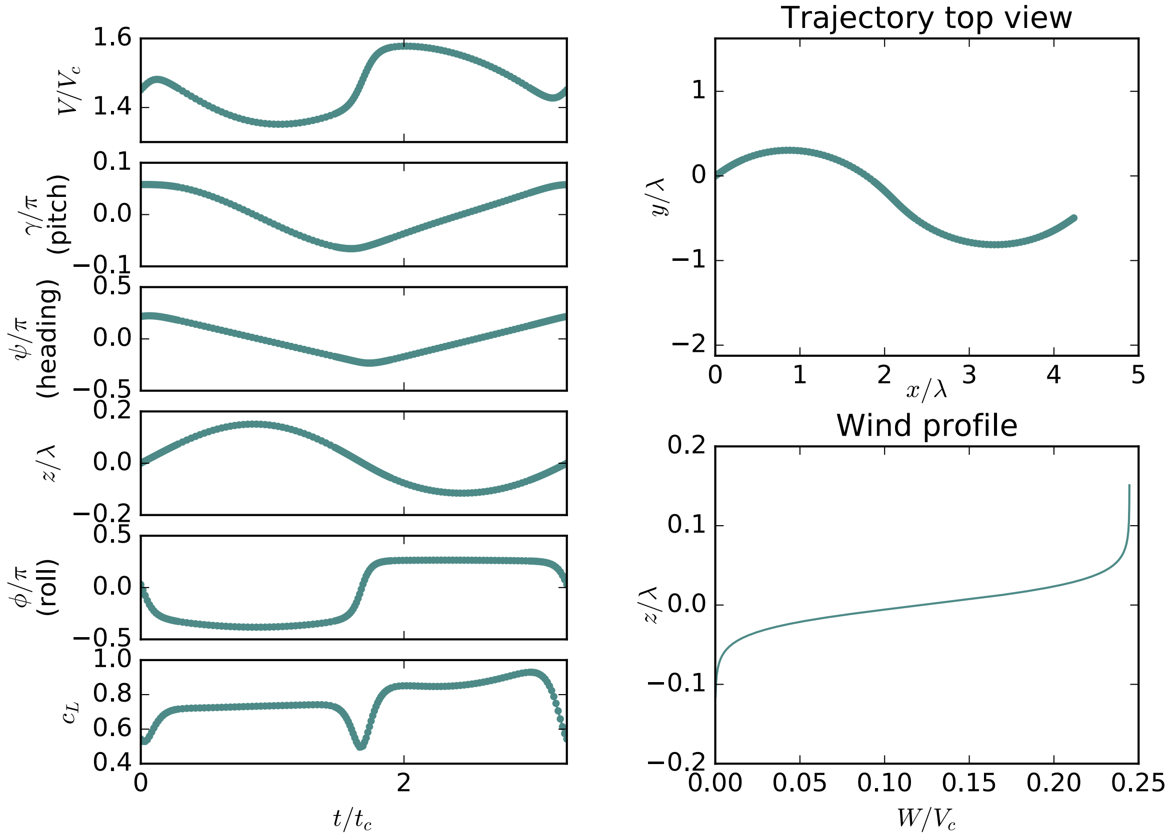

Figure S3: **Solution to the Rayleigh problem** for $f_{\max} = 20, c_{L,f_{\max}} = 0.5, \delta = \lambda/64$. $w_0 = 0.24$.

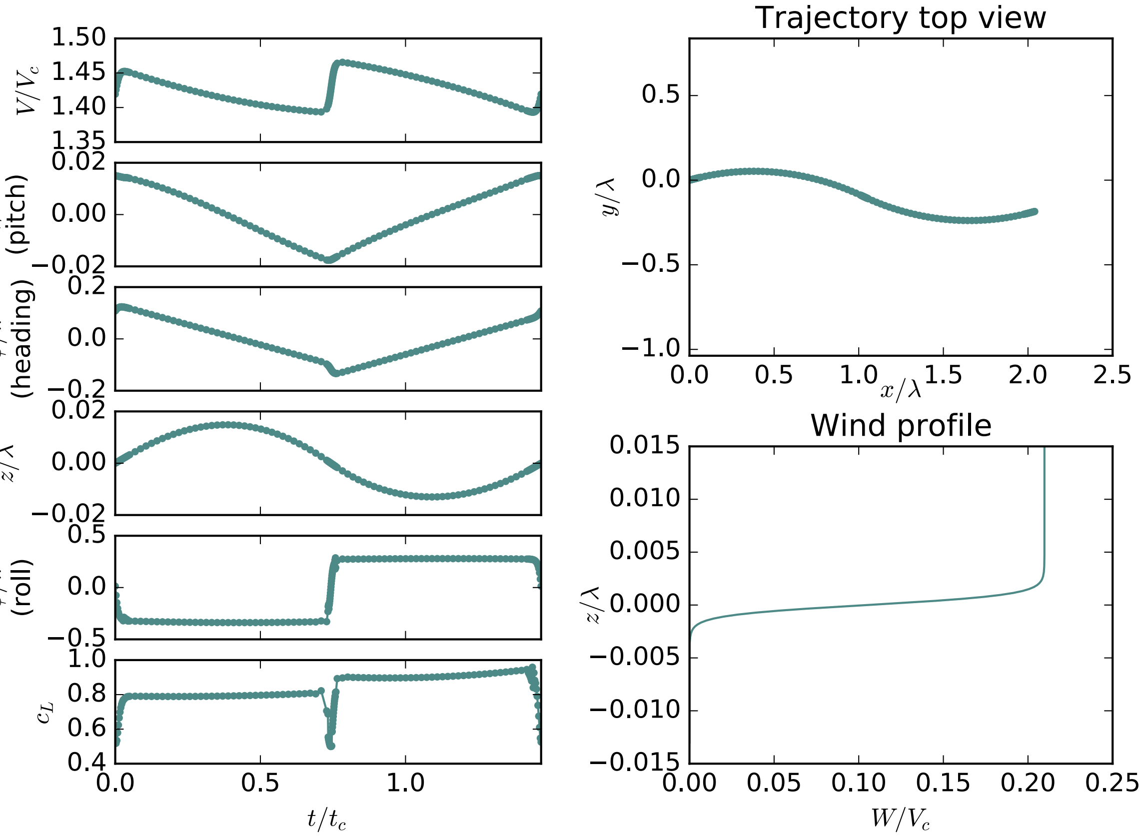

Figure S4: **Solution to the Rayleigh problem** for $f_{\max} = 20, c_{L,f_{\max}} = 0.5, \delta = \lambda/2048$. $w_0 = 0.21$.

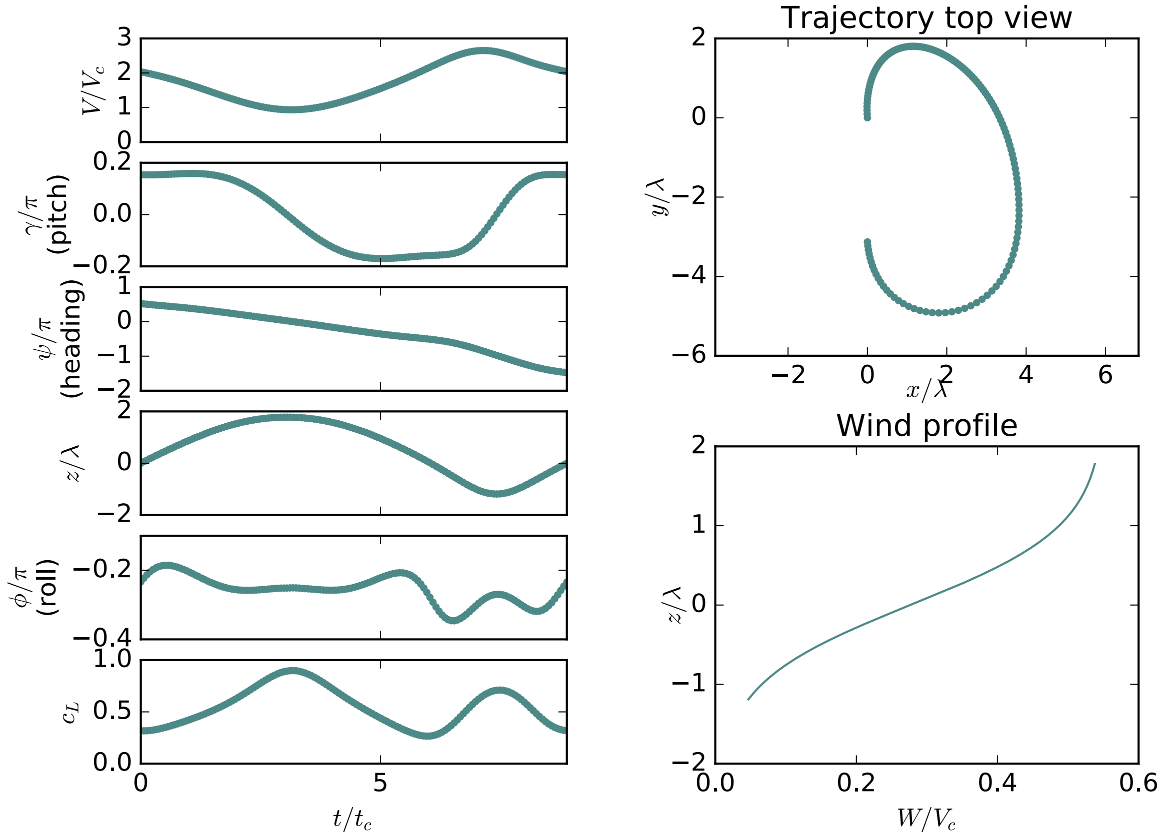

Figure S5: **Solution to the Rayleigh problem** for $f_{\max} = 20, c_{L,f_{\max}} = 0.5, \delta = \lambda/2$. $w_0 = 0.55$.

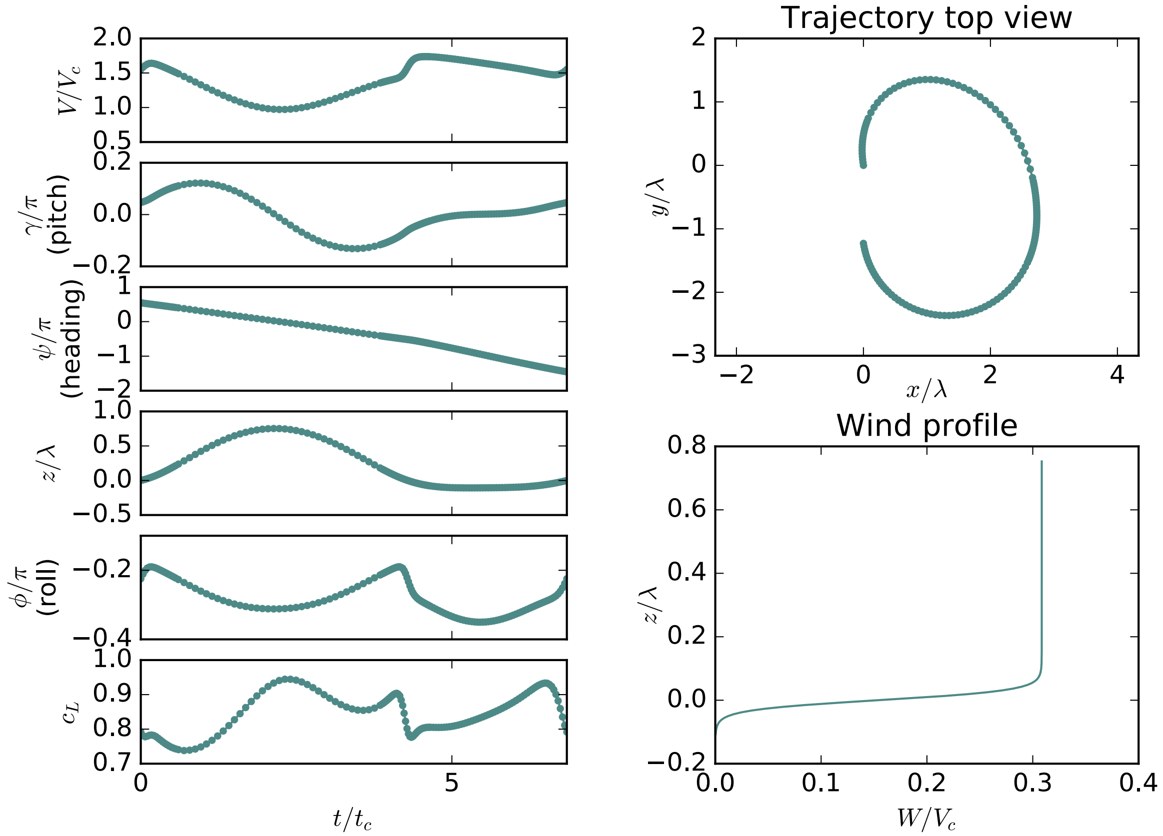

Figure S6: **Solution to the Rayleigh problem** for $f_{\max} = 20, c_{L,f_{\max}} = 0.5, \delta = \lambda/64$, $w_0 = 0.308$.

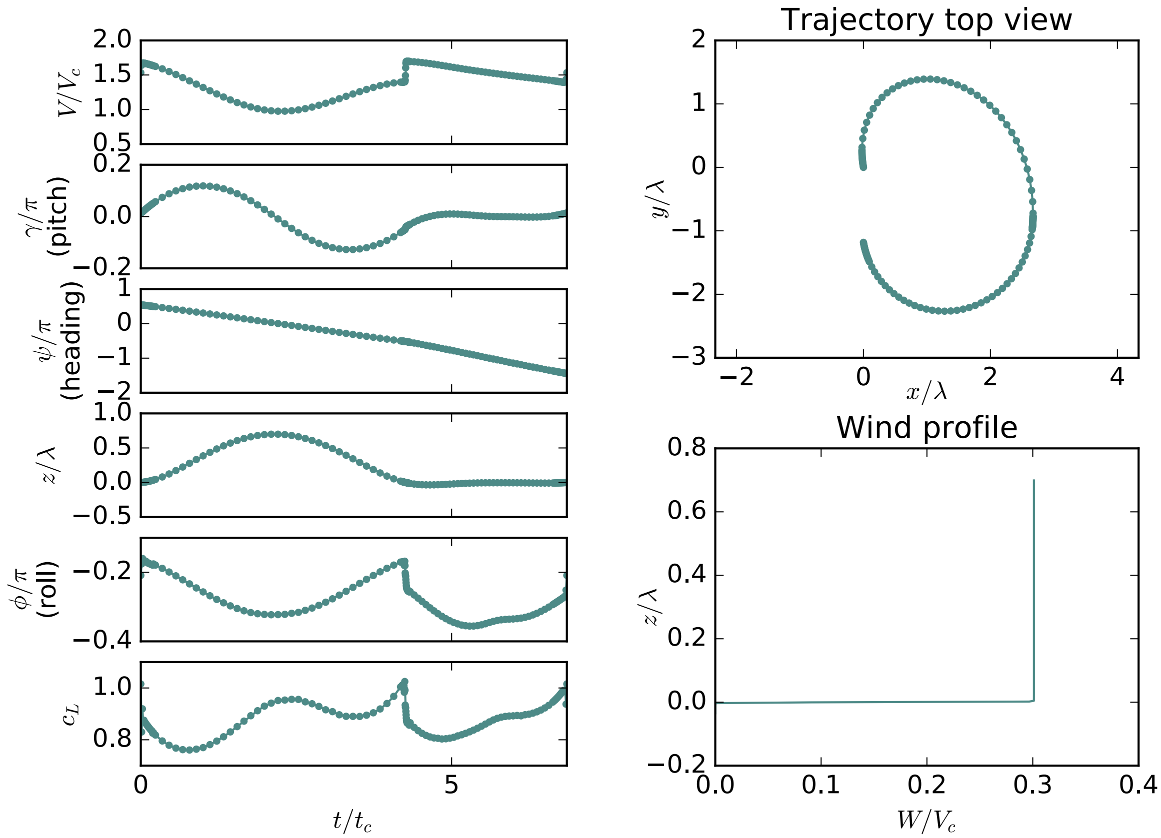

Figure S7: **Solution to the Rayleigh problem** for $f_{\max} = 20, c_{L,f_{\max}} = 0.5, \delta = \lambda/2048$, $w_0 = 0.301$.

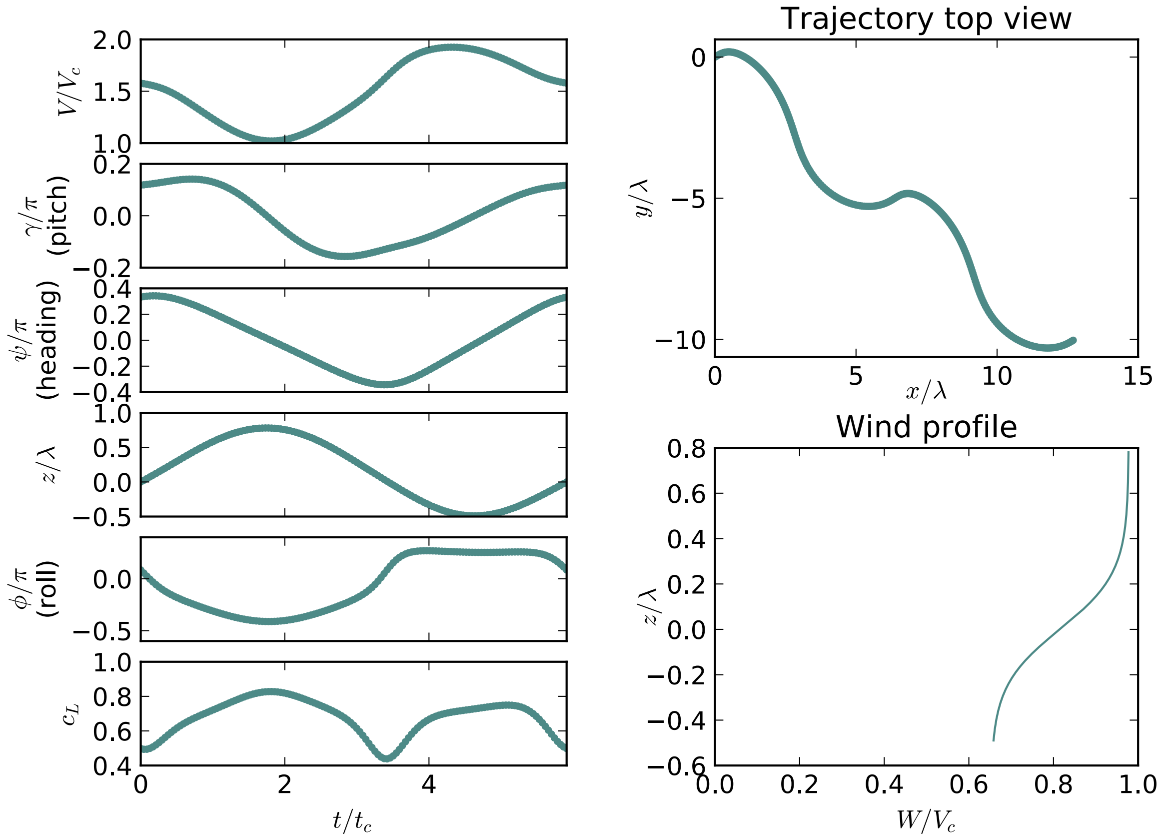

Figure S8: **Solution to the Rayleigh problem** for $f_{\max} = 20, c_{L,f_{\max}} = 0.5, \delta = \lambda/8$, in a wind $W(z) = W_0\left(2 + \frac{1}{1+\exp -z/\delta}\right)$. The constant term in the wind definition, while having no effect on air-relative quantities, illustrates how the trajectory is overall convected downwind if the slow layer has a non-zero velocity.

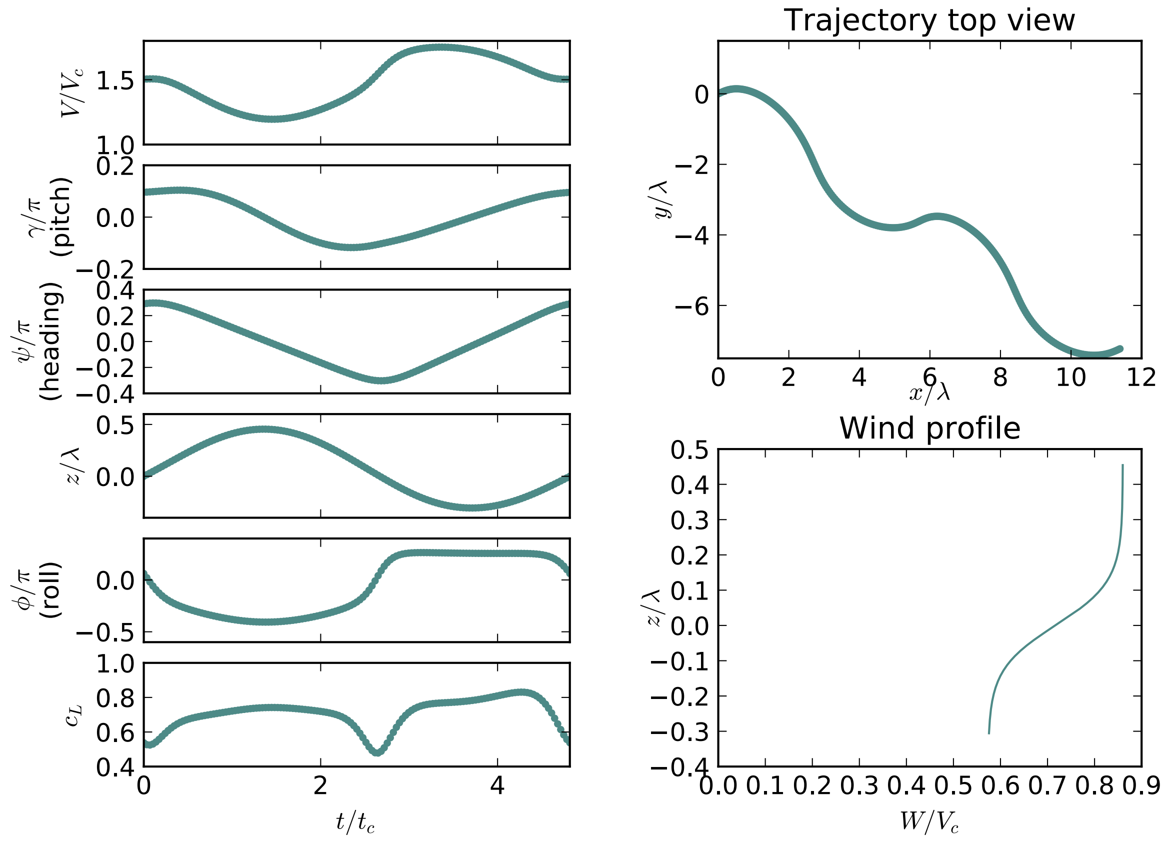

Figure S9: **Solution to the Rayleigh problem** for $f_{\max} = 20, c_{L,f_{\max}} = 0.5, \delta = \lambda/16$, in a wind $W(z) = W_0 \left(2 + \frac{1}{1+\exp -z/\delta}\right)$. The constant term in the wind definition, while having no effect on air-relative quantities, illustrates how the trajectory is overall convected downwind if the slow layer has a non-zero velocity.

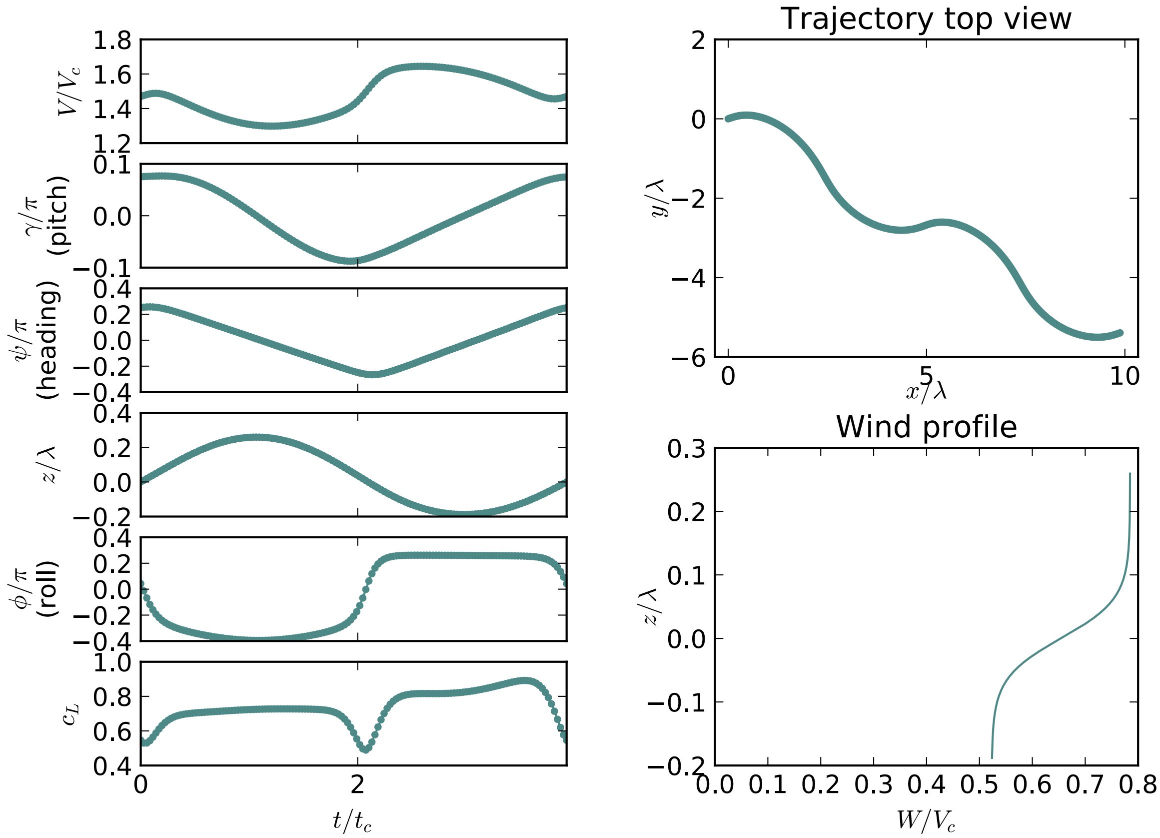

Figure S10: **Solution to the Rayleigh problem** for $f_{\max} = 20, c_{L,f_{\max}} = 0.5, \delta = \lambda/32$, in a wind $W(z) = W_0\left(2 + \frac{1}{1+\exp -z/\delta}\right)$. The constant term in the wind definition, while having no effect on air-relative quantities, illustrates how the trajectory is overall convected downwind if the slow layer has a non-zero velocity.

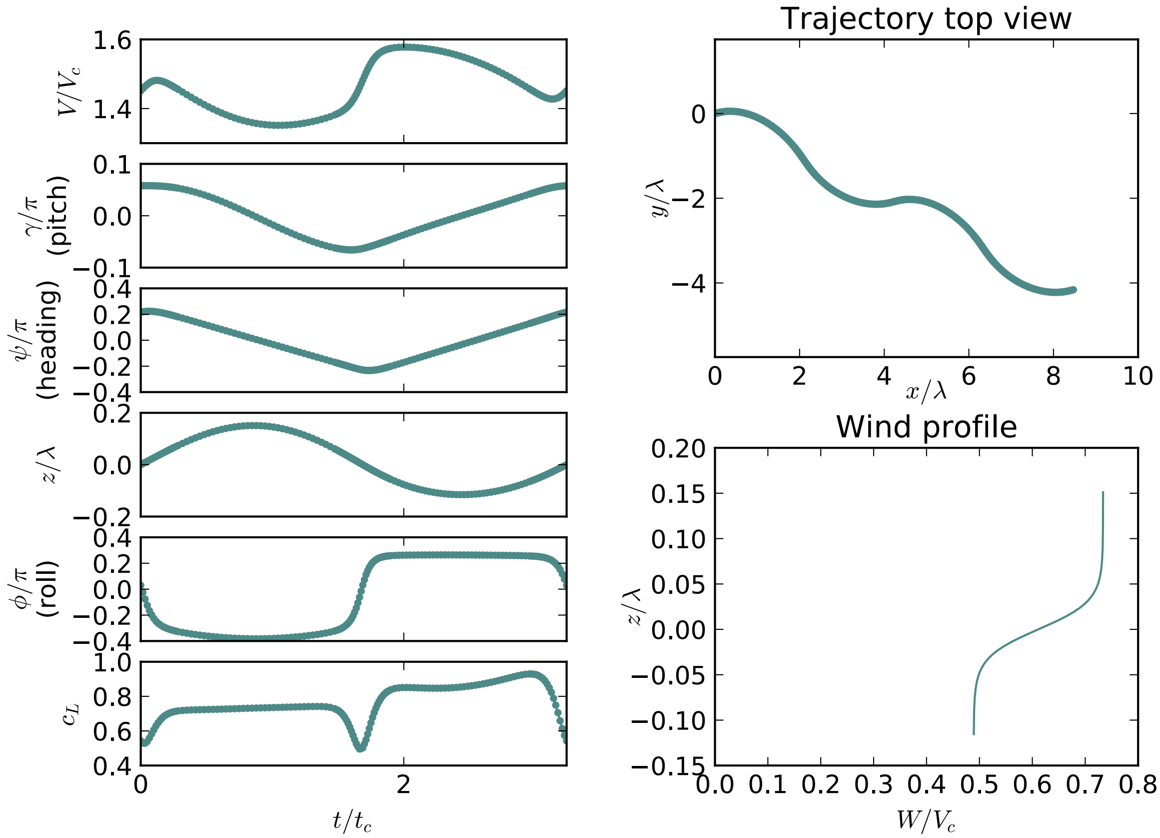

Figure S11: **Solution to the Rayleigh problem** for $f_{\max} = 20, c_{L,f_{\max}} = 0.5, \delta = \lambda/64$, in a wind $W(z) = W_0\left(2 + \frac{1}{1+\exp -z/\delta}\right)$. The constant term in the wind definition, while having no effect on air-relative quantities, illustrates how the trajectory is overall convected downwind if the slow layer has a non-zero velocity.